# Matter waves in time-modulated complex light potentials

S. Bernet,[1] R. Abfalterer,[2] C. Keller,[3] M. K. Oberthaler,[4] J. Schmiedmayer,[2] and A. Zeilinger[3]

[1]*Institut für Medizinische Physik, Universität Innsbruck, Müllerstraße 44, A-6020 Innsbruck, Austria*
[2]*Institut für Experimentalphysik, Universität Innsbruck, Technikerstraße 25, A-6020 Innsbruck, Austria*
[3]*Institut für Experimentalphysik, Universität Wien, Boltzmanngasse 5, A-1090 Wien, Austria*
[4]*Clarendon Laboratory, University of Oxford, Parks Road, Oxford OX1 3PU, United Kingdom*

Temporal light modulation methods which are of great practical importance in optical technology, are emulated with matter waves. This includes generation and tailoring of matter-wave sidebands, using amplitude and phase modulation of an atomic beam. In the experiments atoms are Bragg diffracted at standing light fields, which are periodically modulated in intensity or frequency. This gives rise to a generalized Bragg situation under which the atomic matter waves are both diffracted and coherently shifted in their de Broglie frequency. In particular, we demonstrate creation of complex and non-Hermitian matter-wave modulations. One interesting case is a potential with a time-dependent complex helicity [$V \propto \exp(i\omega t)$], which produces a purely lopsided energy transfer between the atoms and the photons, and thus violates the usual symmetry between absorption and stimulated emission of energy quanta. Possible applications range from atom cooling over advanced atomic interferometers to a new type of mass spectrometer.

PACS number(s): 03.75.Be, 03.75.Dg, 32.80.Pj

## I. INTRODUCTION

The interaction of atomic matter waves with standing light fields has been established as a very useful tool in atom optics. In standing light fields atoms can be trapped, cooled, diffracted, manipulated, and arranged in so called optical lattices [1,2]. The simplicity of the systems recently allowed one to investigate many relevant quantum optical phenomena which are closely related to solid-state physics, like quantum chaotic behavior [3], Bloch oscillations [4], Wannier-Stark ladders and Landau-Zener tunneling [5], spectroscopy of the Bloch bands [6,7], and temporal interference effects [8,9]. An important subgroup of these interactions consists of Bragg scattering of atomic beams at standing light fields [10–14], which can then be viewed in analogy to condensed matter physics as ''crystals of light'' [15]. Atomic Bragg diffraction has been demonstrated at both refractive and absorptive light crystals, revealing interesting features which are analogous to standard Bragg diffraction in crystallography, like Pendellösung-oscillations, anomalous transmission (the Borrmann effect) through absorptive crystals, or the spectral dependence of the scattering phase [12,14,16]. Even the interaction with *complex* light potentials has been investigated [17], resulting in asymmetric Bragg diffraction, i.e., in a lopsided momentum transfer between atoms and photons, which violates an empirical rule called Friedel's law.

In practical applications the coherence of the Bragg scattering process allowed for its use as an efficient coherent beam-splitting mechanism in atom interferometers [18,19], and more recently, as an output coupler for coherent matter waves from a Bose-Einstein condensate of atoms [20,21]. Due to the extremely high momentum and energy selectivity of Bragg scattering, it is also used as a very sensitive spectroscopic tool to investigate such degenerate quantum gases [22]. These methods frequently exploit the possibility to modulate the standing light field in order to get a traveling, or a pulsed light crystal. Thus it becomes important to inves-

tigate in detail the phenomena which arise during the interaction of atomic matter waves with such modulated light fields. One more motivation of our investigations is the success of frequency shifters and sideband modulators in traditional light optics in both scientific and practical applications. Thus we may expect corresponding breakthroughs in matter-wave optics, particularly in combination with the recent advances in the generation of atomic Bose-Einstein condensates which can act as ''atom lasers.''

In previous publications we have already demonstrated that the effect of atomic scattering at traveling Bragg gratings (which arise in an intensity modulated light crystal) results in coherently frequency shifted atomic matter waves. This can be interpreted as an atom-optic analog to an acousto-optic frequency shifter in photon optics [23,24], or as a process of sideband generation similar to radio frequency techniques. In the next sections we will first theoretically and then experimentally investigate this basic effect in more detail.

Furthermore, we extend our investigations to general potential modulations, which can be even complex, and demonstrate how to realize them experimentally with two complementary methods, i.e., either by independently modulating real and imaginary parts of the light potential [25], or by controlling its amplitude and complex phase [26]. Using these methods we realize potential modulations of the form $V \propto \exp(\pm i\omega_M t)$, which represent a complex helix in the time domain. These modulations lead either to a subtraction or to an addition of a quantized energy amount $\hbar \omega_M$ to the kinetic energy of the atomic matter waves, depending on the sign of the exponent.

For an explanation of the observed diffraction effects we present an intuitive Ewald-type model which extends the classical Bragg situation to the case where the crystal is modulated. Such a model allows for the derivation of the new Bragg condition, under which a coupled process of Bragg diffraction and atomic matter-wave frequency shifting

(''atomic sideband generation'') is allowed. For calculating the diffraction efficiencies at the new Bragg angles the results of standard Bragg scattering theory are used, as derived independently in dynamical diffraction theory [27], or in a coupled wave formalism [28], though with additional consideration of the effects of complex, non-Hermitian potentials.

Finally we briefly sketch another viewpoint of our experiments, which points out its relation to recently published interesting experiments, where the Bloch band structure of magneto-optically trapped atoms in optical lattices has been investigated [4–7]. We show that atomic Bragg scattering at modulated potentials can be interpreted as a transition within the energy-band structure of the light crystal, which is induced by the temporal modulation process. Thus our experiments represent a highly sensitive spectroscopic investigation of the energy-band structure (''Bloch bands'') of the light crystal. The main result within this viewpoint is that special types of complex potential modulations, that are actually realized in our experiments, lead to *directed* transitions within the energy bands of the light crystal. This asymmetric energy transfer corresponds to a very unusual interaction between atoms and light fields, which, in particular, does not lead to thermal equilibrium (like, e.g., in blackbody radiation). Besides its fundamental interest, this might have practical applications in atom cooling.

## II. BRAGG DIFFRACTION IN SPACE AND TIME

The interaction of atoms and standing light fields can be described by two complementary pictures. In atomic physics, often an energy-momentum picture is used. There, atoms absorb a photon from one mode of the light field, followed by stimulated reemission to another mode. Thus the atom acquires a momentum change which corresponds to two photon recoil momenta. The process is allowed if the energy of the atom is conserved, i.e., if the absolute value of the atomic velocity does not change in the laboratory frame (supposed that the atom does not change its internal state during the interaction). The efficiency of such an allowed process depends on the probability of the coupled absorption/stimulated emission process, and thus on the light frequency detuning from an atomic transition line. The picture can be generalized for the description of processes, where the atom changes its internal state, or where the atom interacts with light fields of multiple frequencies (''Doppler-sensitive Raman transitions''). There the atom can change both its momentum and its kinetic energy, if a generalized condition of total energy and momentum conservation is fulfilled, which depends on the geometry of the interaction process, on the participating light frequencies, and on the internal state energies. A detailed overview over atom-light interactions in this picture is given in Ref. [29].

In other fields of diffraction physics, e.g., in light and x-ray diffraction, electron, and neutron scattering, often a complementary picture is used which is based on the interaction of an incident wave with a periodic medium. There the diffraction is described according to the Huygens principle as an interference process of all partial waves scattered coherently from the periodic structure. This can be also generalized to a situation where an energy change of the diffracted wave is allowed, if the scattering medium is temporally modulated or moving.

Both the energy-momentum picture and the Huygens picture lead to equivalent results, i.e. to a dynamic diffraction theory. Here we chose the description in the wave picture, resulting in a so-called Ewald construction, which is well known in standard diffraction physics. One advantage is that the allowed diffraction geometry can be constructed directly in the laboratory frame. We generalize this picture to the situation of scattering at a time modulated periodic medium, though with reference to the energy-momentum picture at the end of the paper by pointing out the relation of our experiments to the field of so-called Bloch band spectroscopy.

In general, a light field represents a frequency-dependent *complex* refractive index for the atom [30]. Consequently, an extended standing light field corresponds to a periodic refractive index modulation with the ability to diffract an atomic matter wave—a scattering ''crystal'' made of light. The fact that the scattering of atomic matter waves at such light crystals can be described as a standard Bragg diffraction process, like, e.g., x-ray diffraction at solid crystals, has been well investigated in the literature [10–13]. Analogies have been found even in very fine details [14–16].

The main characteristic of standard Bragg diffraction is a *quantized* momentum exchange between the incident wave and the scattering crystal, which can occur only in multiples of the ''grating momentum'' $\hbar \vec{G}$, where $\vec{G}$ is the grating vector of the crystal with the absolute value $|\vec{G}| = 2\pi/d =: G$, inversely proportional to the grating period $d$. Very similar, a potential which is periodically modulated in the time domain with frequency $\omega_M$ can, under certain circumstances, exchange energy quanta in multiples of $\hbar \omega_M$ with the incident particle. Such an energy exchange, which alters the optical frequency of a scattered photon, or the de Broglie frequency of a scattered particle, is technically described as frequency sideband generation. Due to the analogy between diffraction and sideband generation, both characterized by a quantized exchange of momentum or energy, respectively, the process of sideband generation is sometimes denoted as ''diffraction in time'' [31].

The close analogy between spatial and ''temporal'' diffraction also results in a similar classification of the diffraction regimes. In standard scattering there is a significant difference between diffraction at thin gratings (the Raman-Nath regime) and thick crystals (the Bragg regime). In the Bragg regime the grating is *spatially* thick enough to define a sharply fixed orientation of the grating vector. In a thin grating regime these orientations are undefined in a certain continuous range, allowing for diffraction at a correspondingly continuous range of incidence angles. The borderline is basically given by Heisenberg's position-momentum uncertainty limit.

Similarly, in temporal diffraction the interaction time between the crystal and particle generates two significantly different regimes: a ''short'' (temporal Raman-Nath) and a ''long'' (temporal Bragg) diffraction regime. If the interaction time between the incident particle and a periodically

modulated potential is long enough, energy can only be exchanged in sharply defined energy quanta, whereas in a short (e.g., pulsed light crystal) interaction regime, energy can be exchanged in a continuous range, which allows the generation of spectrally *broad* sidebands. Again the transition between the two regimes is given basically by an uncertainty relation, though now by the time-energy uncertainty.

Linking diffraction in space and time, all combinations of spatial and temporal diffraction regimes can be realized, like, e.g., sharply defined momentum transfer but continuous energy exchange (diffraction of atoms at a pulsed thick light grating in Ref. [13]), corresponding in our terms to a ''spatial Bragg and temporal Raman-Nath regime,'' or continuous momentum transfer and quantized energy exchange (diffraction of atoms and neutrons at vibrating mirrors in Refs. [32] and [33], respectively), corresponding to ''spatial Raman-Nath and temporal Bragg scattering.'' However, all of these combinations exhibit different scattering effects.

In our experiments we investigate coupled spatial diffraction and sideband generation in a spatial and temporal Bragg regime. In contrast to all other combinations this gives rise to new *discrete* Bragg angles, under which the atomic matter waves are simultaneously diffracted and frequency shifted. The periodic light potential for the atoms can be tailored by superimposing different light fields, or by modulating the light frequency across an atomic resonance line. In the following we present an intuitive model for deriving the new Bragg condition for scattering at temporally modulated crystals.

### A. Generalized Ewald construction for modulated crystals

In static Bragg diffraction, an incident wave is scattered only under specific *discrete* incidence conditions—the Bragg angles. This is a consequence of both energy conservation for the incident wave, and quantization of the momentum exchange between crystal and wave in multiples of $\hbar\vec{G}$, where $\vec{G}$ is the grating vector ($|\vec{G}|=2\pi/d$). In the case of a light crystal set up by two counterpropagating light waves with wavelength $\lambda$ and corresponding wave vector $\vec{k}_L$ ($|\vec{k}_L|=2\pi/\lambda$), the grating constant $d$ corresponds to $\lambda/2$, and the grating vectors are $\vec{G}=\pm 2\vec{k}_L$.

Energy conservation and quantized momentum exchange are the basis of the well-known Ewald construction, where the tips of incident and scattered wave vectors are located on a common circle around their origin (equal length corresponding to energy conservation); additionally, they are connected by a grating vector (corresponding to a quantized momentum change of $\hbar\vec{G}$). A construction for first-order Bragg diffraction, corresponding to a momentum exchange of exactly $\hbar\vec{G}$ is sketched in Fig. 1(a). Obviously, for a given length of the incident wave vector $\vec{k}_A=m\vec{v}_A/\hbar$ (where $m$ and $\vec{v}_A$ are the atomic mass and velocity, respectively), for diffraction at the $n_G$th order, the Ewald construction yields only one possible incidence angle; the Bragg angle $\theta_{B,n_G}$, satisfying
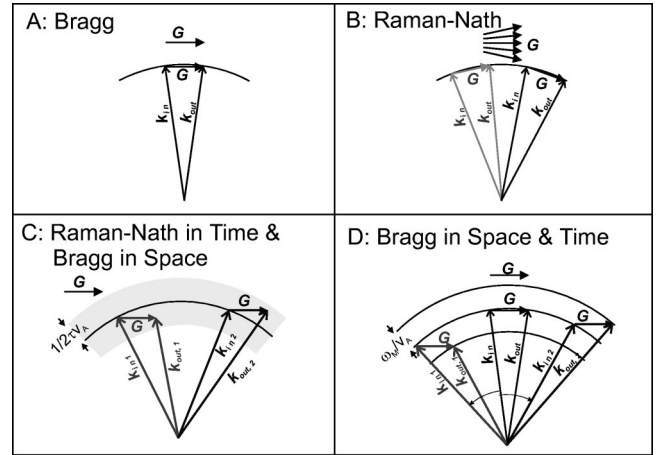


FIG. 1. Ewald constructions for different situations of first-order scattering at a given direction (''to the right side''). The discussed cases are (A) a thick static grating, (B) a thin static grating, (C) a thick pulsed grating, and (D) a thick, harmonically modulated grating.

$$\sin(\theta_{B,n_G})=n_G\frac{|\vec{G}|}{2|\vec{k}_A|}. \tag{1}$$

However, since the grating vector is usually not oriented, i.e., it exists in both opposite directions, the orientations of incident and scattered wave vectors can be exchanged, which yields two symmetrically arranged Bragg angles for scattering at the two conjugate $\pm n_G$th Bragg orders.

The situation changes in the case of scattering at a focused standing light wave (thin grating), as sketched in Fig. 1(b). Due to focusing in the $z$ direction, the $z$ component of the grating vector, $G_z$ is no longer defined sharply, but has an uncertainty in an angular range inversely proportional to the size of the focus $\Delta G_z \approx (2\Delta z)^{-1}$ [34]. Although the condition of energy conservation (elastic scattering) still holds, the *direction* of the transferred grating momentum can now be chosen in a certain continuous range, and the Ewald construction yields a corresponding range of incidence angles where elastic diffraction is possible. As an example, two allowed pairs of incident and scattered wave vectors are sketched in Fig. 1(b). Thus, focusing of a transversely extended (plane) standing light wave results in a continuous transition from a Bragg regime, where scattering appears only at discrete incidence conditions, to a thin-grating regime (the Raman-Nath regime), where a broad range of incidence angles (and momenta) is scattered [35].

The Ewald construction can be generalized to the situation of a temporally modulated crystal. Such a temporal modulation provides the possibility to transfer kinetic energy to the scattered wave. If the interaction time $\tau$ is short (the ''temporal Raman-Nath regime''), e.g., by pulsing the light crystal, then there results a continuous energy uncertainty $\Delta E_{kin}\approx\hbar/\tau$ of the scattered wave, which enables Bragg diffraction at much less stringent incidence conditions. This is demonstrated in Fig. 1(c) by a modified Ewald construction where the circle of the original Ewald construction is substituted by a circular band with a thickness of $1/\tau v_A$, corre-

sponding to an energy uncertainty of $\Delta E_{kin} \approx \hbar/\tau$. Similar to the spatial Raman-Nath situation of Fig. 1(b), diffraction is now again allowed for a whole range of incidence angles. However, in contrast there is now a *fixed momentum transfer* between incident and outgoing wave vectors, accompanied by a *continuous energy transfer*. Thus the length of the scattered wave vector can change, and scattering becomes inelastic. As mentioned above, such a situation might be characterized as a spatial Bragg regime and a temporal Raman-Nath regime.

However, in our experiment we stay in a spatial and temporal Bragg regime by employing a temporally harmonic modulation with frequency $\omega_M$, and allowing for a sufficiently long interaction time $\tau$ (several modulation periods). Now the energy exchange between the crystal and wave is quantized in multiples of $\hbar\omega_M$, with an uncertainty inversely proportional to the interaction time ($\Delta E_{kin} \approx \hbar/\tau$). Consequently, both momentum and energy transfer between crystal and wave are quantized. The Ewald construction, modified for this situation, is sketched in Fig. 1(d). Now the peak of the incident wave vector defines the radius of the middle circle. The lengths of the atomic wave vectors shifted by the quantized energy offsets $\pm\hbar\omega_M$ are given by new circles with smaller and larger radii, offset by $\omega_M/v_A$. A sharply defined grating vector $\vec{G}$ connects incident and outgoing wave vectors, which, however, can now lie on the different circles. Obviously, these conditions are satisfied only for discrete incidence angles, although there are now three possibilities for first-order diffraction in one direction, as indicated in the figure. The situation thus corresponds to a generalization of Bragg scattering to the time domain. Consequently, the standard static Bragg condition results as a special case setting $\omega_M=0$. The waves scattered at the new incidence angles are expected to be coherently frequency shifted by the modulation frequency of the crystal. Note that in our situation of scattering at a Bragg crystal, the diffracted beam contains only one single-frequency component at a time, because only a certain frequency shift, which depends on the incidence angle, can fulfill the generalized Bragg condition derived above. This means that a modulated Bragg crystal indicates the frequency shift of a diffracted atom by a unique Bragg angle. Thus, in the spatial and temporal Bragg regime, a modulated crystal acts simultaneously as a sideband generator and an analyzer.

### B. Calculation of the generalized Bragg condition

In order to calculate the new Bragg angles for diffraction with quantized energy exchange we analyze the situation sketched in Fig. 1(d). Both momentum and energy can only be changed by quantized amounts, requiring

$$\vec{k}'_A = \vec{k}_A + n_G\vec{G},$$

$$(2)$$

$$\frac{\hbar|\vec{k}'_A|^2}{2m} = \frac{\hbar|\vec{k}_A|^2}{2m} + n_M\hbar\omega_M.$$

There $n_M$ and $n_G$ are the numbers of frequency modulation quanta $\hbar\omega_M$ and grating momenta $\hbar\vec{G}$, exchanged between wave and crystal, and thus correspond to the temporal and spatial diffraction orders, respectively. $\vec{k}_A$ and $\vec{k}'_A$ denote the incident and diffracted atomic wave vectors. An additional condition is imposed by the fact that each exchange of a modulation quantum (i.e., each ''diffraction process in time'') has to be accompanied by an exchange of a grating momentum (i.e., a spatial diffraction process), in contrast to spatial diffraction, which can also happen without energy exchange (''standard'' Bragg diffraction).[1] Therefore, the possible temporal diffraction orders $n_M$ are restricted by the spatial diffraction order $n_G$ to only three cases:

$$n_M=0 \quad \text{or} \quad n_M=\pm n_G. \quad (3)$$

This means that there is always the possibility for elastic scattering ($n_M=0$) or, that there is the possibility to exchange a number of energy quanta corresponding to the spatial diffraction order ($n_M=\pm n_G$).

For solving Eqs. (2) it can be exploited that due to momentum conservation only the component of the atomic wave vector $k_{A,\|}$ parallel to the grating vector can change, but not the perpendicular component $k_{A,\perp}$ [this is also straightforwardly seen from the geometry sketched in Fig. 1(d)]. This means that

$$k'_{A,\perp} = k_{A,\perp},$$

$$k'_{A,\|} = k_{A,\|} + n_G G, \quad (4)$$

$$\frac{\hbar k'^2_{A,\|}}{2m} = \frac{\hbar k^2_{A,\|}}{2m} + n_M\hbar\omega_M.$$

These equations can be solved easily. As an abbreviation we introduce the matter-wave frequency of an atom, $\omega_A = \hbar|\vec{k}_A|^2/2m$, and the two-photon recoil frequency $\omega_{Rec} = \hbar|\vec{G}|^2/2m$ an atom acquires with respect to its original rest frame after addition of one grating vector $\vec{G}$. Thus $\omega_{Rec}$ is a geometric constant of the setup. As a result, for the parallel components of an allowed pair of incident and diffracted wave vectors we obtain

$$k_{A,\|} = \frac{1}{2}n_G G\left(\frac{n_M\omega_M}{n_G^2\omega_{Rec}} - 1\right),$$

$$(5)$$

$$k'_{A,\|} = \frac{1}{2}n_G G\left(\frac{n_M\omega_M}{n_G^2\omega_{Rec}} + 1\right),$$

and

---

[1] This is a consequence of the Schrödinger equation, where spatial and temporal coordinates are not symmetric.

$$|\vec{k}_A'| = |\vec{k}_A| \sqrt{\frac{n_M \omega_M}{\omega_A} + 1}. \qquad (6)$$

Thus an incidence angle $\theta_{In}$, where an incoming atom can be scattered, is

$$\sin(\theta_{In}) = \frac{k_{A,\|}}{|\vec{k}_A|} = \frac{n_G |\vec{G}|}{2|\vec{k}_A|} \left( \frac{n_M \omega_M}{n_G^2 \omega_{Rec}} - 1 \right)$$

$$= \sin(\theta_{B,n_G}) + \frac{n_M \omega_M |\vec{G}|}{2 n_G \omega_{Rec} |\vec{k}_A|}. \qquad (7)$$

Obviously, the relation is a generalization of the static Bragg condition, yielding the static Bragg angle in the case of an unmodulated crystal ($n_M = 0$).

Similarly, the angle of the scattered atom, $\theta_{Out}$, is given by

$$\sin(\theta_{Out}) = \frac{k_{A,\|}'}{|\vec{k}_A'|} = \frac{n_G |\vec{G}|}{2|\vec{k}_A|} \frac{\left( \dfrac{n_M \omega_M}{n_G^2 \omega_{Rec}} - 1 \right)}{\sqrt{1 + n_M \omega_M / \omega_A}}$$

$$= \frac{\sin(\theta_{In}) - 2 \sin(\theta_{B,n_G})}{\sqrt{1 + n_M \omega_M / \omega_A}}. \qquad (8)$$

In our experimental situation of very small incidence and scattering angles (below 200 $\mu$rad), all the sinus functions can be replaced by their arguments. Therefore, from Eq. (7), in a very good approximation, we obtain the difference $\Delta\theta$ of the new Bragg angles $\theta_{In}$ (with frequency shift) from the original static Bragg angles, $\theta_{B,n_G}$, for the cases where Eq. (3) holds, i.e., $n_M = \pm n_G$:

$$\Delta\theta = \theta_{In} - \theta_{B,n_G} = \pm \theta_B \frac{\omega_M}{\omega_{Rec}}. \qquad (9)$$

There $\theta_B = G/2k_A$ is the static Bragg angle for first-order diffraction. This shows that the angular offset of a new Bragg angle from the static Bragg angle, obtained at a modulated crystal, is a direct measure of the frequency shift acquired by the scattered atoms. Therefore, a modulated Bragg crystal is able to produce sidebands of matter waves, and, simultaneously, to identify the frequency offset of the sidebands by their offset from the static Bragg angle. This relation will be used in several parts of our experiment.

Additionally, our experimentally applied modulation frequencies are far below the matter-wave frequency $\omega_A$ of the incident atoms. Considering this, from Eqs. (7) and (8) we obtain the total scattering angle of the atoms as $\theta_{Out} - \theta_{In} = 2\theta_{B,n_G}$, which is identical to the scattering angle of static Bragg diffraction. Additionally, according to Eq. (7), the angular offset of the new allowed incidence angles from the static Bragg angle does not depend on the diffraction order (assuming $n_M = \pm n_G$), i.e., the incidence angles of all atoms frequency shifted by $n_G \hbar \omega_M$ are offset by the same amount. This shows that the total far-field diffraction pattern of

frequency-shifted atoms looks exactly like the diffraction pattern in ''static'' Bragg diffraction, though with an angular offset given by Eq. (9). The situation thus resembles scattering at a moving crystal, which would result in a scattering of frequency-shifted atoms with a diffraction pattern looking like a static diffraction picture, although centered around a new incidence angle. In fact, in a previous publication an interpretation based on atomic scattering at traveling subcrystals within the modulated light crystal was introduced [23].

However, for many situations another picture is advantageous. An alternative Bragg condition can be derived by considering the ondulation or ''wobbling'' frequency, $\omega_{Wob}$, with which an atom incident at one of the new Bragg angles $\theta_{In}$ traverses the grating planes of a crystal:

$$\omega_{Wob} = v_A \sin(\theta_{In}) |\vec{G}| = -\frac{n_M}{n_G} \omega_M + n_G \omega_{Rec}. \qquad (10)$$

If we take into account the additional condition $n_M = \pm n_G$ [Eq. (3)] for diffraction with energy exchange, this can be rewritten as

$$n_G^2 \hbar \omega_{Rec} = n_G \hbar (\omega_{Wob} \pm \omega_M). \qquad (11)$$

This central equation can be used as an alternative formulation of the Bragg condition [Eq. (7)] for inelastic scattering at modulated crystals. An interpretation is straightforward if the atom is regarded in its *incident rest frame*. There the energy of the atom is zero. However, after a static Bragg scattering process, the atom moves. The corresponding kinetic energy of the atom *with respect to the original rest frame* can only be supplied from a time-dependent modulation ''seen'' by the atom in its frame. In fact, even in static scattering the atom experiences a light intensity modulation with frequency $\omega_{Wob}$ due to the apparently moving light crystal (with respect to the atomic rest frame), and therefore can change its kinetic energy in multiples of $\hbar \omega_{Wob}$. An alternative interpretation of the static Bragg condition now results from the requirement that this energy change must match the atom's recoil energy $n_G^2 \hbar \omega_{Rec}$, linked to the addition of $n_G$ grating momenta (i.e., $n_G$th-order diffraction) to the resting atom (note that the quadratic dependence of the recoil energy on the diffraction order is due to the matter-wave dispersion relation in vacuum). This means that the static Bragg condition for matter-wave scattering can be reformulated as $n_G^2 \hbar \omega_{Rec} = n_G \hbar \omega_{Wob}$.

However, if the crystal is temporally modulated with a frequency of $\omega_M$, the atom experiences this frequency contribution in addition to the ondulation frequency $\omega_{Wob}$. These two (''spatial'' and temporal) frequency contributions result in beating frequencies of $\omega_{Wob} \pm \omega_M$, corresponding to new modulation quanta which can be exchanged between the atom and crystal. Therefore, the meaning of Eq. (11) is that the recoil frequency for $n_G$th-order diffraction ($n_G^2 \hbar \omega_{Rec}$) has to match a multiple of the new energy quantum $\hbar(\omega_{Wob} \pm \omega_M)$ which can be exchanged between the atom and crystal. This alternative formulation of the Bragg

condition is particularly useful for discussing the angular and velocity selectivity of the inelastic Bragg diffraction, as will be shown below.

### C. Diffraction efficiency at Bragg incidence

In the next step we investigate the efficiency of sideband production. In the Ewald picture of Fig. 1, this might be seen as a determination of the weights of the different circles, which then represent the wave-vector magnitudes of elastically and inelastically scattered atoms. In this short discussion we will limit ourselves to the situation of scattering at first order. For static first-order Bragg scattering, it can be shown that the amplitude of the diffracted wave function, $A$, is given by [10,12,16,28]

$$A = \sin\left(\frac{\pi \Delta z}{L}\right). \qquad (12)$$

There $L$ is the so-called Pendellösungs length depending on the grating constant $d$, on the atomic recoil energy $E_{Rec} = \hbar^2 G^2/2m$, and on the coefficient $V_G$ of the spatial Fourier transform of the grating potential $V$, which corresponds to the amplitude of the grating component with period $d$:

$$L = \frac{d E_{Rec}}{V_G \sin(\theta_B)}. \qquad (13)$$

Obviously, the diffracted amplitude oscillates between $-1$ and $1$ as a function of the crystal length, $\Delta z$, or of the grating amplitude. This is denoted as the so-called ''Pendellösung.'' However, if scattering is only limited to low-diffraction efficiencies well below the first Pendellösungs length (this condition is fulfilled in many of our experiments), it is possible to expand Eq. (12):

$$A \approx \frac{\pi \Delta z}{L}. \qquad (14)$$

The corresponding diffraction efficiency $P$, i.e., the ratio of diffracted atoms to incident atoms, is then given by the squared modulus of Eq. (14):

$$P \approx \left(\frac{\pi \Delta z}{L}\right)^2. \qquad (15)$$

The situation changes if the potential is additionally modulated in time. Now a two-dimensional Fourier transform has to be performed, dividing the total potential in contributions with grating constants $n_G G$ and modulation period $n_M \omega_M$, i.e.,

$$V(x,t) = \sum \sum V_{n_G,n_M} \exp(in_G Gx - in_M \omega_M t). \qquad (16)$$

The amplitude of first-order Bragg scattering at a subgrating with grating vector $n_G G$, modulated with one of the frequencies $n_M \omega_M$ within the temporal Fourier spectrum of the modulation, is now given by inserting the respective Fourier
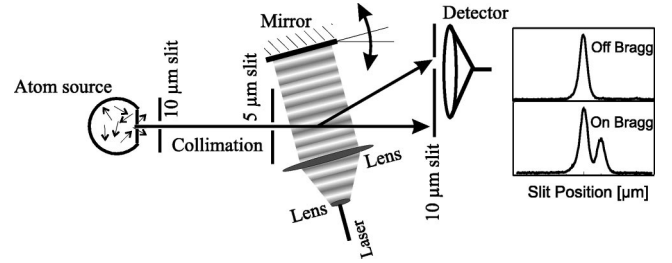


FIG. 2. Experimental setup (not to scale). A collimated thermal beam of metastable argon atoms crosses a standing light wave. The diffraction pattern can be registered with spatial resolution by scanning a narrow slit in front of the extended channeltron detector. The laser light intensity is modulated in some parts of the experiment using an acousto-optic modulator (AOM). The two graphs show the results for off-Bragg incidence (only one peak of transmitted atoms) and Bragg incidence (a second peak of Bragg-diffracted atoms arises) in the case of an unmodulated laser beam. Additionally, the scattering efficiency can be registered as a function of the atom's incidence angle at the light crystal by fixing the detection slit at the position of the diffraction peak and tilting the retroreflection mirror.

components $V_{n_G,n_M}$ into Eq. (12), under the assumption that the atomic incidence occurs under the corresponding Bragg angles [given by Eq. (7)].

Specifically, the diffraction efficiencies for first-order spatial diffraction at the basic grating with the exchange of zero (elastic scattering) or one modulation quanta are

$$P_{n_G=1,n_M=0} = \left(\frac{\pi \Delta z \sin(\theta_B)}{E_{Rec} d}\right)^2 |V_{1,0}|^2,$$

$$P_{n_G=1,n_M=\pm 1} = \left(\frac{\pi \Delta z \sin(\theta_B)}{E_{Rec} d}\right)^2 |V_{1,\pm 1}|^2, \qquad (17)$$

respectively.

There it is assumed that the condition of small diffraction efficiencies holds, such that the approximation of Eq. (15) can be applied. The first term of each equation only contains geometric constants of the setup. Thus it turns out that the diffraction efficiencies depend only on the squared modulus of the coefficients of a two-dimensional (spatial and temporal) Fourier transform. This dependence will be confirmed in Sec. III.

### III. EXPERIMENTS

We start by describing the scheme of our experiment [36]. Then we will demonstrate the basic features of scattering at time-modulated crystals, before investigating the effects of complex potential modulations.

### A. Setup

Our setup is sketched in Fig. 2. Argon atoms in a metastable state are diffracted at a standing light wave, followed by spatially resolved detection.

The argon atoms are first excited to a metastable state (lifetime $> 30$ s) in a gas discharge. Only these metastables

can be detected by our ''channeltron'' detector, by releasing their high excitation energy (12 eV) in a collision with the detector surface. The beam of metastable argon atoms emerges into the high vacuum chamber, with an average velocity of 700 ms$^{-1}$, and a thermal velocity distribution of 60% (full width at half maximum). The beam is collimated by a set of two slits (first slit 10 $\mu$m, second slit 5 $\mu$m, distance 1.4 m) to a divergence of less than 5 $\mu$rad, i.e., considerably better than the diffraction angle of $2\theta_B \approx 36$ $\mu$rad.

After collimation the atoms enter a 5-cm-long interaction region with a standing light field, set up by retroreflecting the central part of a collimated, expanded laser beam at a mirror (surface flatness <50 nm), located in the vacuum beamline. The frequency of the diode laser is actively locked at an open atomic transition of metastable argon (at 801.7 nm) using saturation spectroscopy. The frequency can be shifted by a well-defined offset using an acousto-optic frequency shifter. Both the intensity and frequency of the laser can be modulated with rates up to 200 kHz, using an acousto-optic switch, or by directly modulating the diode laser current, respectively. Details of the light crystal generation vary in the different parts of the experiment, and are explained below.

The standing light field represents a light crystal with a generally complex index of refraction for the atoms. Thus the atomic beam is diffracted if its incidence angle is a Bragg angle, but not affected at arbitrary incidence. The crystal angle can be controlled by tilting the retroreflection mirror with a piezo actuator.

In the far field behind the crystal, at a distance of 1.4 m, the diffraction pattern can be spatially resolved by scanning a third 10-$\mu$m slit in front of the large area ''channeltron'' detector. However, in most of the experiments the detection slit is just located at the position of a Bragg diffraction peak, and the diffraction efficiency is then measured as a function of the mirror angle (''rocking curves''). Note that even in the case of modulated light crystals, the detection slit position remains on the same position, since both the direction of the incident beam and the total diffraction angle are always constant.

### B. Interaction of metastable argon atoms with light fields

Obviously, the whole experiment depends on the interaction between the argon atoms and the light field. The corresponding theory is well established, and thus we point out only features important for our actual experiments.

A light field represents a positive, a negative, or even an imaginary potential for an atom, depending on the detuning of the light frequency from an atomic transition line. Interaction of atoms with detuned light gives rise to the well-known dipole potential. The spectral shape of the potential is a typical dispersion curve, as displayed in Fig. 3. Its spectral dependence is given by [30]

$$V_{real}(\omega) = \frac{\hbar\Omega_{Rabi}^2}{4} \frac{\omega - \omega_0}{(\omega - \omega_0)^2 + (\gamma/2)^2}. \qquad (18)$$
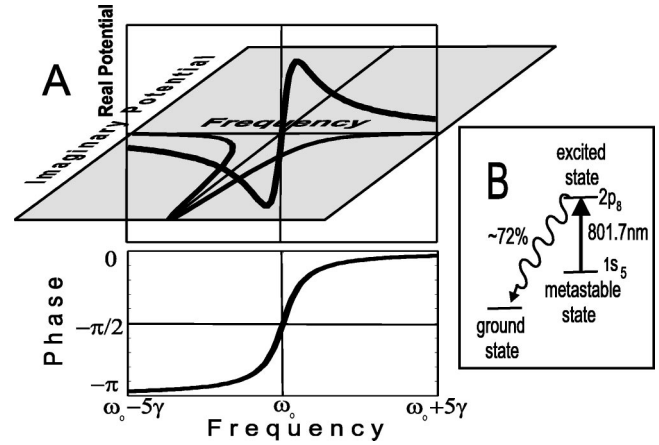


FIG. 3. Complex potential of a light field for an atom near an open atomic transition line. The real part corresponds to the dipole potential, with the spectral shape of a dispersion line centered at the transition frequency. The (negative) imaginary part corresponds to ''absorption'' of the atoms, realized by pumping to the (undetected) ground state. Its spectral shape corresponds to a Lorentzian. Below, the complex phase angle is drawn as a function of the light frequency. It has the shape of an arctangent function with an offset of $-\pi/2$.

$\Omega_{Rabi} = DE/\hbar$ is the Rabi frequency of the population oscillations between the two levels with a transition dipole moment $D$, driven by the electrical strength of the light field $E$ at resonance; $\omega_0$ is the center frequency of the transition line, and $\gamma$ is the effective line width of the transition.

From quantum mechanics it is known that an external potential changes the phase velocity of a wave function. Due to the fact that such a spectrally dependent phase change acts as a spectral filter on matter waves, it has to satisfy certain causality requirements defined by the Kramers-Kronig relations. They demand that a dispersion shaped spectral dependence of a real potential has to be accompanied by a Lorentz-shaped imaginary contribution:

$$V_{imag}(\omega) = -i\frac{\hbar\Omega_{Rabi}^2}{4} \frac{\gamma/2}{(\omega - \omega_0)^2 + (\gamma/2)^2}. \qquad (19)$$

Such an imaginary potential corresponds to an absorption coefficient with a Lorentzian spectral profile. In fact, such an imaginary contribution is contained in the interaction between atoms and light fields, since resonant excitation of an atom consequently leads to spontaneous emission of a photon, which kicks the atom out of its path—i.e., the atom is effectively removed from its original state (similarly, absorption of a light beam in a material can be due to diffuse scattering). However, since in a two-level atom at optical frequencies the deflection due to diffuse scattering of a photon is smaller than the detector angular resolution, this deflection is typically not resolved in Bragg diffraction experiments. The situation changes in our three-level argon atom. For realizing detectable ''absorption,'' the most important feature of the metastable $1s_5$ atoms is their *open* transition $1s_5 \rightarrow 2p_8$ ($4s[3/2]2 \rightarrow 4p[5/2]2$) at 801.7 nm (the effective line width is $\approx 9$ MHz). If the atoms are excited at this

wavelength, they decay spontaneously with a branching ratio of 72% to the ground state which is not detected by our channeltron, i.e., the atoms are absorbed with respect to our measurement.

Both real and imaginary parts of the potential can be combined in a resulting complex potential:

$$V(\omega) = \frac{\hbar \Omega_{Rabi}^2/4}{\omega - \omega_0 + i\gamma/2}. \tag{20}$$

Figure 3(A) shows the complete *complex* potential of a light field for an atom near an absorption line, split into the Lorentzian imaginary part and the dispersion profile of the real part.

The arctangent-shaped complex phase angle of the potential is plotted below as a function of the light frequency. This spectral shape of the phase angle is important, since it determines the phase of the diffracted atoms. This is due to the fact that, in the case of a complex potential, the Pendellösung length becomes complex [Eq. (13)], and the complex potential phase then directly determines the phase of the scattered wave according to Eq. (14). This behavior was experimentally verified earlier [15], and investigated in detail in Ref. [16]. Interesting theoretical investigations of matter-wave Bragg scattering at complex potentials were presented in Refs. [37,38]. The most important aspect for our actual experiments is the fact that the phase of the scattered wave can be adjusted in a range from $-\pi$ to 0 by changing the light frequency from the far red detuned side to the far blue detuned side of an atomic transition.

### C. Diffraction at modulated real light potentials

The basis of our investigations is the fact that a modulated light crystal produces new Bragg peaks, and that the atoms in these new peaks are coherently shifted by the modulation frequency $\omega_M$ to higher or lower matter-wave frequencies. The coherence of the frequency shifting process was already demonstrated in a previous publication [24]. Here we demonstrate quantitative investigations about the angular dependence, peak width, and velocity selectivity of the diffraction process, in order to verify our Ewald-type diffraction model. We also investigate a special case where Bragg diffraction at a modulated crystal occurs at a perpendicular incidence of the atoms, a situation which can be never achieved in standard static Bragg scattering. This special situation might have practical applications as a sensitive method for mass spectroscopy.

#### 1. Intensity-modulated light crystal

In the first experiment combining spatial and temporal Bragg diffraction, an atomic beam was scattered at a light crystal which was periodically switched on and off. Although this situation was already investigated in Refs. [23,24], here we briefly present the basic effects. Typical results of such an experiment are shown in Fig. 4.

In that figure we compare the efficiencies of first-order Bragg diffraction as a function of the atomic incidence angle for two cases of an unmodulated light crystal (upper graph),
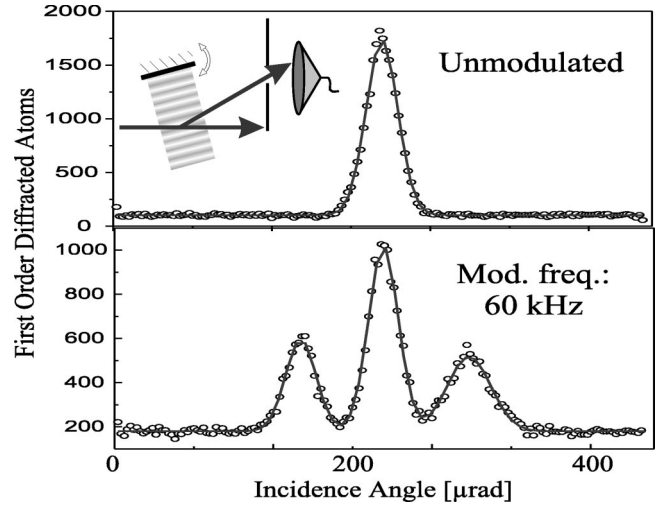


FIG. 4. Generation of new Bragg peaks at a modulated crystal: In the upper graph, the efficiency of first-order Bragg diffraction at an *unmodulated* light crystal is plotted as a function of the atomic incidence angle (''rocking curve,'' see inset), i.e., the angle of the retroreflection mirror (the solid line is a Gaussian fit to the data). Only one peak of diffracted atoms appears at the Bragg angle. In the lower graph the measurement is repeated, using an intensity-modulated light crystal, which is switched on and off periodically with a frequency of $\omega_M = 2\pi \times 60$ kHz. Two new peaks arise at new incidence angles. They are arranged symmetrically around the static Bragg peak at the center. Note the slight difference in the widths of the new peaks.

and a periodically intensity modulated light crystal (lower graph). The light frequency was detuned far enough ($\approx 10$ linewidths) from the open transition at 801.7 nm such that the potential could be assumed to be purely real. The experiment was performed by locating the detection slit at the position of the first diffraction order, and then detecting the number of diffracted atoms as a function of the retroreflection mirror angle. In the case of an unmodulated crystal we obtained only one peak of diffracted atoms at the static Bragg angle. This is a typical result demonstrating that our measurements were performed in the Bragg diffraction regime (note that the result of such a measurement in the case of diffraction at a *thin* grating would consist in an almost constant efficiency, i.e., without any angular dependence).

In the next experiment (lower graph), the light crystal was switched on and off periodically with a modulation frequency of $\omega_M = 2\pi \times 60$ kHz. As a result we found two new peaks of Bragg scattered atoms, arranged symmetrically around the static Bragg peak. In a previous publication it was shown that these peaks consist of atoms whose matter-wave frequency is *coherently* shifted by the modulation frequency [24]. This was demonstrated by interferometric superposition of the diffracted frequency shifted matter wave with the transmitted unshifted wave, resulting in traveling interference fringes, which were detected. The sign of the frequency shift depends on the side on which the new peaks arise with respect to the central Bragg peak. Frequency-upshifted atoms appear at positions closer to perpendicular incidence, and vice versa. According to Eq. (9) the angular separation $\Delta\theta$ from the static Bragg angle is proportional to the modulation
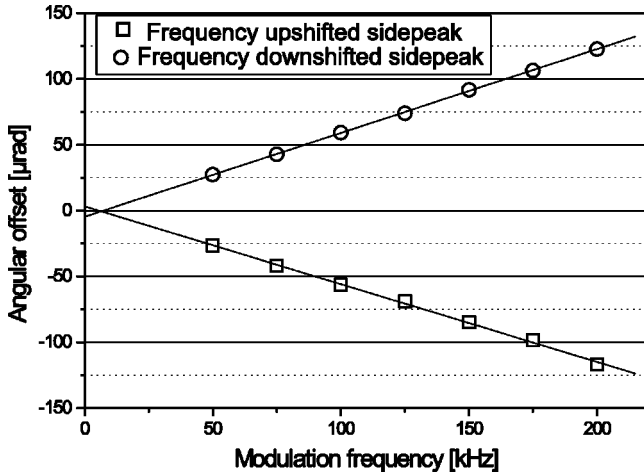
FIG. 5. Offset of the two new Bragg peaks (see Fig. 4, lower graph) from the static Bragg angle as a function of the intensity modulation frequency. The linear behavior expected from Eq. (9) is clearly demonstrated.

frequency ($\Delta\theta/\theta_B = \pm\omega_M/\omega_{Rec}$, where $\omega_{Rec} = \hbar|\vec{G}|^2/2m = 2\pi \times 30$ kHz). This relation is verified in a sequence of experiments where the modulation frequency was changed in a range from 25 to 200 kHz, and "rocking curves" were recorded in the same way as before. In Fig. 5 the position of the new Bragg peaks is plotted as a function of the modulation frequency.

The graph clearly demonstrates the linear behavior of the angular offset of the new Bragg peaks from the static Bragg angle. The absolute values of the corresponding slopes obtained from the data ($s = 0.61 \pm 0.01$ $\mu$rad kHz$^{-1}$) agree with the expected value [Eq. (9): $s = \theta_B/\omega_{Rec} = 0.60$ $\mu$rad kHz$^{-1}$] within the experimental resolution (inserting the experimentally measured Bragg angle of 18 $\mu$rad, which corresponds to an average atomic velocity of 690 ms$^{-1}$).

As an additional test of our model, we examined the widths of the new Bragg peaks at different modulation frequencies. From our previous theoretical considerations, it is expected that the peak width increases with increasing modulation frequency, due to the broad longitudinal velocity distribution of the atoms in the beam. The reason for this is most easily seen from the alternative Bragg condition for modulated crystals, formulated in Eq. (11). This condition is imposed on the two new Bragg peaks, frequency shifted by $\pm\omega_M$ for first-order spatial diffraction ($n_G = 1$), and requires $\omega_{Wob} = \omega_{Rec} \pm \omega_M$, respectively. Since both the intensity modulation frequency $\omega_M$ and the recoil frequency $\omega_{Rec}$ are constants, the only dispersive parameter depending on the atomic velocity and on the incidence angle is the "wobbling" frequency $\omega_{Wob}$ with which the atoms rattle across the grating planes, given by $\omega_{Wob} = 2\pi|\vec{v_A}|\sin(\theta)/d$, where $\theta$ is the incidence angle of the atoms, and $|\vec{v_A}|$ is the modulus of the atomic velocity. A first-order Taylor expansion then shows, that the wobbling frequency has a certain width $\Delta\omega_{Wob}$, depending on the width of the velocity distribution $\Delta|v_A|$:

$$\Delta\omega_{Wob} = \frac{2\pi\Delta|v_A|}{d}\sin(\theta). \qquad (21)$$

This relation shows that the width of the wobbling frequency, and correspondingly the size of the angular incidence range, around which the alternative Bragg condition [Eq. (11)] can be fulfilled, depends on both the corresponding incidence angle $\theta$, where the new Bragg peaks are centered, and on the broad velocity distribution $\Delta|v_A|$ ($\approx 350$-ms$^{-1}$ full width at half maximum) of the atomic beam. With increasing incidence angle, and thus with increasing modulation frequency, the dependence from the velocity distribution becomes larger, increasing the width of the new Bragg peaks in the "rocking curves." The same relation also reveals that the two peaks of frequency-shifted atoms appearing in each rocking curve (like in Fig. 4) should have different widths. Note that this asymmetry between the widths of the left and right peaks is already visible in the data of Fig. 4. The reason for this is that the two new Bragg peaks arise at different absolute incidence angles [see Eq. (9)] $\theta_{\pm 1} = \theta_B(1 \pm \omega_M/\omega_{Rec})$. Therefore, the width of the wobbling frequency distribution, and accordingly the angular range $\Delta\theta$ in which Eq. (11) is fulfilled, becomes different for the left and right peaks, respectively:

$$\Delta\theta_{\pm 1} \approx \frac{d}{2\pi|v_A|}\Delta\omega_{Wob} = \frac{\Delta|v_A|}{|v_A|}\theta_B(1 \pm \omega_M/\omega_{Rec}). \qquad (22)$$

In fact, the widths of the peaks are not symmetric. A special case with the most pronounced asymmetry is obtained if the modulation frequency corresponds to the recoil frequency. In this case the angular width of one of the two peaks should not be influenced by the velocity distribution at all ($1 - \omega_M/\omega_{Rec} = 0$), whereas the other peak should show a doubled velocity dependence ($1 + \omega_M/\omega_{Rec} = 2$) with respect to the static peak width obtained by setting $\omega_M = 0$ in Eq. (22).

In Fig. 6 the width of the peaks in the rocking curves is plotted as a function of the incidence angle at which the new peaks are centered. The graph agrees with the behavior expected from our model [Eq. (22)]. The individual data points for the left (negative angles) and right peaks (positive angles) are taken at different modulation frequencies (the same data set as used for Fig. 5); however, the width is not plotted as a function of the modulation frequency but as a function of the corresponding incidence angles. First, the data show that the peak width increases with increasing incidence angle (modulation frequency), in accordance with Eq. (21). Second, the graph shows that a minimum of the width is obtained at perpendicular incidence of the atoms, and not at Bragg incidence (the two linear lines are drawn to indicate the center of symmetry). Thus the width of the peaks does not depend directly on their angular distance to the static Bragg peak, but rather on the absolute incidence angle. In the next section, we pay some special attention to the extreme case where Bragg diffraction occurs at perpendicular incidence.
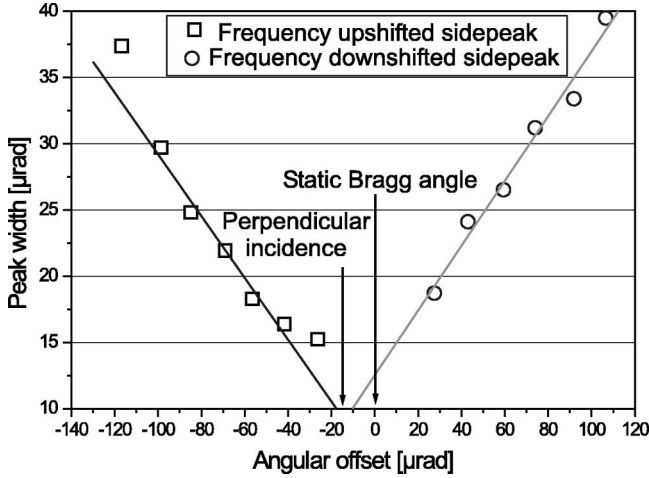
FIG. 6. Angular width of the new Bragg peaks as a function of the incidence angles belonging to different modulation frequencies (same data set as in Fig. 5). Negative and positive angles correspond to the left and right peaks of frequency-downshifted and -upshifted atoms, respectively. With increasing modulation frequency, and correspondingly growing incidence angle, the peak width enlarges, due to the increased dependence on the broad longitudinal velocity distribution of the atomic beam. The plot also shows that the broadening of upshifted and downshifted diffraction peaks is almost symmetric with respect to the *perpendicular incidence direction* (indicated in the plot), and not with respect to Bragg incidence (zero angular offset). In particular, the minimal peak width is not obtained for static diffraction (i.e., for atoms which are incident at the static Bragg angle), but for atoms which are frequency upshifted by 30 kHz, corresponding to exactly perpendicular incidence.

### 2. Bragg diffraction at perpendicular incidence

In ''normal'' static experiments the Bragg condition can never be fulfilled at perpendicular incidence of a wave at a crystal. The situation changes, however, in the case of a time-modulated potential. In order to be diffracted the atoms have to ''feel'' a potential modulation in their rest frame, which is equal to the two-photon recoil frequency [Eq. (11)]. This modulation can be produced either by the atomic rattling across the grating planes ($\omega_{Wob}$), or by an externally applied intensity modulation ($\omega_M$), or by a beating of both ($\omega_{Wob} \pm \omega_M$). This viewpoint suggests that at perpendicular incidence, where the incident atoms move parallel to the grating planes and therefore the ''rattling'' frequency $\omega_{Wob}$ vanishes, the necessary modulation must be delivered by the externally applied intensity modulation, i.e., $\omega_M = \omega_{Rec}$. Due to symmetry considerations, no diffraction direction can then be preferred and scattering is expected to occur with equal intensities at the two conjugate first diffraction orders. Thus the diffraction pattern resembles one obtained at a thin grating, since the typical asymmetry of the Bragg diffraction patterns is repealed (typically only one peak of diffracted atoms is expected, as, e.g., shown in Fig. 2).

Since the recoil frequency is equal for all atoms, independent of their velocity, and since additionally the wobbling frequency vanishes for all atoms, there should be no velocity selectivity of the Bragg diffraction process [this is also sug-

gested by Eq. (22) setting $1 - \omega_M / \omega_{Rec} = 0$]. Thus, different diffraction efficiencies can only be due to different interaction times with the light crystal.

Experimental investigations of Bragg diffraction at perpendicular incidence are plotted in Fig. 7. In the experiment we recorded far-field diffraction patterns for various atomic velocities by scanning the detection slit. The velocities were selected using a time-of-flight method, where the gas discharge of the atomic source was pulsed (pulse width 0.5 ms) and the atomic intensities were recorded as a function of their arrival time at the detector, at a distance of $\approx 2.9$ m from the source. In the first experiment [Fig. 7, graph (a)] the crystal was adjusted for perpendicular incidence of the atomic beam, and the light crystal was unmodulated. As expected for static Bragg diffraction, (almost) no scattered atoms were registered. Some remaining scattering is due to the limited angular collimation of our beam, and to the limited Bragg selectivity of our crystal. Both restrictions become more important for faster atoms, and therefore some higher ''background'' is measured there. In Fig. 7(b) the same experiment was performed, though now we modulated the intensity of our light crystal with the recoil frequency $\omega_{Rec} = 2\pi \times 30$ kHz. As expected from our model, the data show a symmetric diffraction of atoms at the two conjugated first diffraction orders. The matter-wave frequency of the atoms in both new Bragg peaks is shifted by the modulation frequency in the same direction, that is to higher absolute values. The diffraction efficiency shows only a small dependence on the atomic velocity. This becomes especially evident when compared to a more general situation of Bragg scattering at modulated crystals, as presented in Fig. 7(c). There we chose an ''arbitrary'' modulation frequency of 75 kHz, and adjusted the corresponding new incidence angle for frequency-downshifted atoms, that is $\approx 60$ $\mu$rad. The corresponding diffraction patterns show the typical feature of Bragg diffraction, i.e., there appears only one peak of diffracted atoms. Additionally, the diffraction efficiency depends strongly on the atomic velocity. A comparison of the diffraction efficiencies as a function of the atomic velocities for perpendicular incidence, for Bragg incidence, and for incidence at $\approx 60$ $\mu$rad is presented in Fig. 8.

In this figure the difference in the velocity dispersion of (elastic and inelastic) diffraction processes at increasing absolute incidence angles becomes obvious. In particular, the minimal velocity selectivity of Bragg diffraction at a modulation frequency of 30 kHz, and the increased velocity dependence of elastic scattering and of scattering at much higher modulation rates (0 kHz and 75 kHz in the figure) is in agreement with Eq. (22).

The independence of the diffraction condition at perpendicular incidence, $\omega_M = \omega_{Rec} = 2h/m\lambda^2$, from parameters like atomic velocity, light intensity, and interaction potential, also suggests an interesting application. In fact, the modulation frequency $\omega_M$ at which the new Bragg peaks appear depends only on the atomic mass, and on the light wavelength which can be measured very accurately, and which can be chosen arbitrarily in a broad range in the vicinity of a transition line (real potential), as long as a small interaction
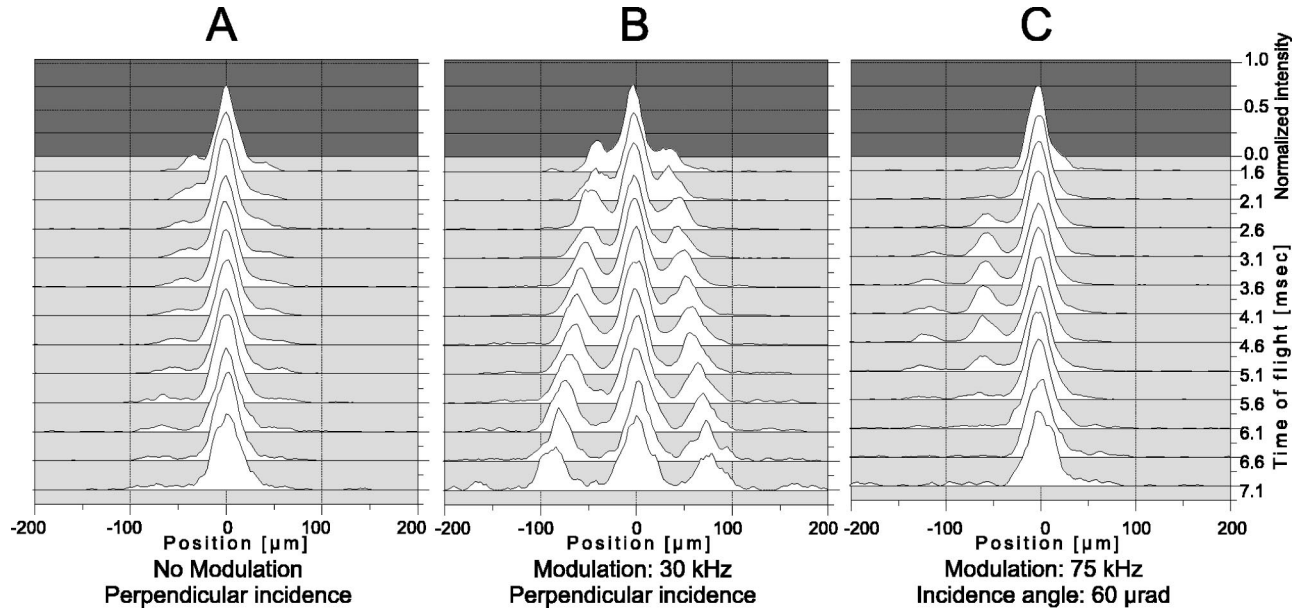
FIG. 7. Bragg diffraction at perpendicular incidence: The graphs show far-field diffraction patterns (recorded by scanning the detection slit) for atoms with different velocities (time of flight through our beam line). (A) is taken for an unmodulated light crystal at perpendicular incidence of the atoms. Only the peak of transmitted atoms in the center of each scan is obtained, with almost no diffracted atoms, since the Bragg condition can never be fulfilled at perpendicular incidence. In (B), the light crystal was modulated with the atomic recoil frequency of 30 kHz, again at perpendicular incidence. Now atoms are diffracted symmetrically to both sides of the central peak of transmitted atoms. Although the experiment was performed in the Bragg regime, the results are similar to diffraction patterns of a thin grating, and the diffraction efficiency shows only a small dependence on the atomic velocity. In (C) a more ''general'' situation of scattering at modulated crystals is investigated for comparison. There, a modulation frequency of 75 kHz was applied, and the atomic incidence angle was adjusted to one of the two new corresponding Bragg angles at $\approx 60$ $\mu$rad. Now, as expected for the Bragg case, the diffraction patterns show only one peak of scattered atoms, and the diffraction efficiency depends strongly on the atomic velocity.

potential between the atoms and the light exists. This might imply a practical application as a highly sensitive method of mass spectroscopy, e.g., in the case of a molecular beam, by measuring the intensity modulation frequency at which diffraction of a collimated, perpendicularly incoming beam is observed. The accuracy of the method can be significantly improved by increasing the interaction time between the particles and the light crystal, using a slower beam or a thicker crystal. For larger molecules, where the modulation frequency would be very low, the resolution of the method can be improved by observing diffraction into higher spatial Bragg orders $n_G > 1$ (i.e., larger deflection angles), which requires a correspondingly higher modulation frequency $n_G \omega_{Rec}$.

The basic experiments demonstrated so far are the foundation for the advanced investigations, which will be presented in the next section. Mainly, they confirm our model, and the usefulness of the alternative formulation of the Bragg condition in Eq. (11) for the diffraction of frequency-shifted atoms. This frequency shifting can be interpreted as a sideband generation of the matter waves. However, in contrast to typical situations of sideband generation (e.g., in the radiofrequency technique) in our case the diffracted beams generally contain only one frequency component at a time. This means that a modulated Bragg crystal cannot only be used to shift the frequency of diffracted atoms, but also to indicate their frequency shift by the corresponding new Bragg

angles.[2] This feature will now be applied for investigating the sideband structure generated by unconventional (even non-Hermitian) potential modulations.

### D. Diffraction at complex modulated light potentials

In the preceding section we demonstrated the basic effect of atomic matter-wave frequency shifting by diffraction at an intensity-modulated light crystal. We now extend our investigations to complex temporal modulation schemes where both real and imaginary parts of the potential, or its amplitude and complex phase, are manipulated independently. There we use the fact that by adjusting the laser frequency we can change our potential within a range of positive and negative real values, to imaginary values. This will be used to Fourier synthesize specific temporal modulation functions of the potential. According to our model [Eq. (17)], the Fou-

---

[2]In contrast, in a thin grating regime the effect of frequency shifting (or sideband generation) would also be possible; however, then all sidebands would appear simultaneously in the diffracted beams. Such an experiment in the Raman-Nath regime would lose the feature to indicate the sideband generation, e.g., a spatially resolved far-field diffraction picture would not reveal the sideband structure. However, in our case of a combined spatial and temporal Bragg regime our modulated crystal acts simultaneously as both a sideband generator and an analyzer.
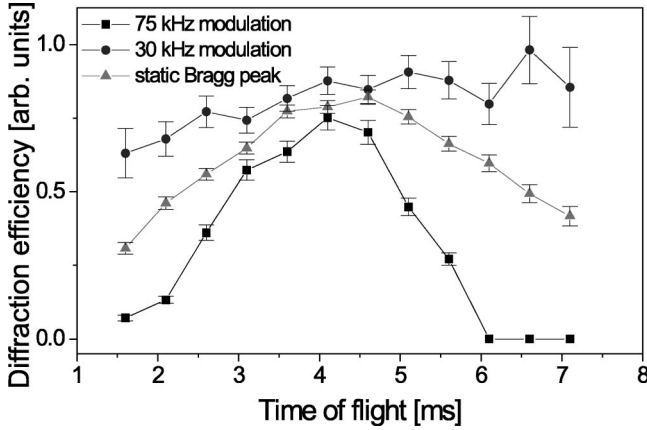
FIG. 8. Velocity selectivity of Bragg diffraction at intensity modulated light crystals. The efficiencies of first-order Bragg diffraction are plotted as a function of the atomic velocity for three different modulation frequencies (0, 30 kHz, and 75 kHz). In one case the modulation frequency was equal to the recoil frequency (30 kHz), and the corresponding incidence angle of the atoms was perpendicular to the light crystal. In the other case an ''arbitrary'' modulation frequency of 75 kHz was chosen, and the corresponding new Bragg angle of scattering of frequency-downshifted atoms of 60 $\mu$rad was adjusted. The middle curve shows the diffraction efficiency of elastically scattered atoms, incident at the static Bragg angle. Obviously, the data taken at a modulation frequency of 30 kHz shows the smallest dependence on the atomic velocity. The residual velocity dependence is due to the increasing interaction time, but not to a velocity selectivity of the diffraction process. In contrast, the data taken at 0- and 75-kHz modulation frequencies show a larger dependence on the velocity, due to the growing influence of the longitudinal velocity distribution at higher absolute incidence angles.

rier coefficients should directly determine the ability of our modulated crystal to create sidebands of the corresponding frequencies. For the sideband detection we use the fact that, according to Eq. (9), the appearance of a new Bragg angle automatically indicates the corresponding frequency offset of the diffracted atoms.

### *1. Complex light potential with temporal helicity*

In this experiment we exploit the fact that it is possible to tailor potentials by superimposing light from different lasers. We start from the same setup as in the previous experiments (Fig. 2); though now we use two diode lasers to create the light crystal [25]. The light of the two lasers is first collinearly superposed at a beam-splitter cube. Then the two combined beams enter the same collimation optics as before. This results in two exactly coinciding light crystals generated in front of the retroreflection mirror.[3] However, the intensities of the two lasers can now be modulated independently

---

[3]The light crystals can be regarded as exactly coinciding at the position where the atomic beam passes. The reason is that the maximal experimentally used frequency difference is on the order of 100 MHz, resulting in a spatial beating period of 1.5 m, whereas the distance of the atomic beam to the mirror surface is only 2 mm.

using for each laser a separate acousto-optic modulator (AOM) for periodically switching their intensity. In the experiments we used the same modulation frequencies for both lasers, though with an adjustable temporal phase relation. This could be achieved by using two function generators with one common time basis to drive the two AOM's.

Using different frequency detunings of the two light crystals from resonance, and additionally, using different relative modulation phases, we can generate a potential of the form

$$V(x,t) = (1 + \cos(Gx))[V_{L1}(1 + \cos(\omega_M t))$$
$$+ V_{L2}(1 + \cos(\omega_M t + \phi_t))]. \quad (23)$$

The first term of the equation describes a fully modulated spatial grating, which is formed in front of the mirror surface, whereas the second term describes the applied temporal modulation. There it is assumed that the temporal intensity modulation of the two lasers is harmonical and fully modulated. The independent variables which can be controlled in our experiment are the individual crystal potentials $V_{L1}$ and $V_{L2}$, and the relative temporal phase $\phi_t$ between the two harmonic potential modulations, which can be adjusted directly at the frequency generators driving the AOM's. The crystal potentials can be chosen real (positive and negative) or imaginary (only negative) by adjusting the light frequencies. The absolute values of the potentials can be controlled by changing the corresponding light intensities.

In the experiment the absolute values of the two potentials where always equalized by adjusting the light intensity of the two individual crystals independently for equal relative diffraction efficiencies, i.e., $|V_{L1}| = |V_{L2}|$. Therefore, we can set

$$V_{L1} := V_0,$$

$$\quad (24)$$

$$V_{L2} := V_0 \exp(i\phi_c).$$

$V_0$ is the potential of the first laser, and $\phi_c$ is the complex potential phase difference depending on the difference of the two laser detunings from resonance (see Fig. 3). In order to calculate the Bragg diffraction efficiencies for first-order elastic Bragg scattering, and sideband production of positive or negative order (corresponding to positive or negative frequency shift), a two-dimensional (temporal and spatial) Fourier analysis of the total potential has to be performed, according to Eq. (16). The Fourier coefficients $V_{n_G=1,n_M=0}$ and $V_{n_G=1,n_M=\pm 1}$, then determine the first-order diffracted wave *amplitudes* for elastic and inelastic scattering, respectively. The corresponding diffraction efficiencies are then proportional to the squares of these Fourier coefficients, according to Eq. (17) (valid for small efficiencies). Fortunately, such a two-dimensional Fourier transform is easily performed in the case of harmonic potential modulations. Since spatially and temporally dependent functions are just multiplied in Eq. (17), the time-dependent and spatial Fourier transforms can be separated. The two-dimensional transform is then just the product of the two individual ones. The spatial part of Eq. (17) describes a normal potential grating with well-known Bragg diffraction properties, i.e., it enables diffraction at the

positive or negative first diffraction orders. In our case we are only interested in the sideband generation efficiencies of the first spatial diffraction order (as detected in our ''rocking curves''), such that it is sufficient to analyze only the temporal part of the modulation. This can be done easily by substituting all cosine functions according to $\cos(a) = (\exp(ia) + \exp(-ia))/2$. Evaluation of the products and sorting the terms then yields

$$V(x,t) = V_0(1 + \cos(G \cdot x))\{(1 + \exp(i\phi_c))$$
$$+ \tfrac{1}{2}[1 + \exp(i(\phi_c + \phi_t))\exp(i\omega_M t)]$$
$$+ \tfrac{1}{2}[1 + \exp(i(\phi_c - \phi_t))\exp(-i\omega_M t)]\}. \quad (25)$$

This indicates that we have a ''normal'' static Bragg grating (first term) of modulus $|V_0(1 + \exp(i\phi_c))|$, and two time-modulated components with absolute values of $|V_0[1 + \exp(i(\phi_c + \phi_t))]|/2$, and $|V_0[1 + \exp(i(\phi_c - \phi_t))]|/2$, producing frequency-downshifted and -upshifted sidebands, respectively. In a typical ''rocking curve'' as in Fig. 4, the squared modulus of these three components determines the intensities of the center peak, and the negative and positive sideband peaks, respectively:

$$P_{1,0} \propto |V_0[1 + \exp(i\phi_c)]|^2,$$
$$(26)$$
$$P_{1,\pm 1} \propto |V_0[1 + \exp(i(\phi_c \pm \phi_t))]/2|^2.$$

Here it should be mentioned that for technical reasons the modulations actually applied were not harmonic, but rectangular functions (the lasers were switched on and off). This results in additional Fourier components of higher order. However, the first of these components is already the third harmonic of the modulation frequency, leading to new peaks in the rocking curves which are far separated from the investigated peaks of first-order sidebands, and thus do not disturb the measurements.

In order to verify the predictions of Eq. (26) for the diffraction efficiencies, we chose different frequency detunings ($\phi_c$) and modulation phases ($\phi_t$) of the two superimposed light crystals, both intensity modulated with a frequency of $\omega_M = 2\pi \times 100$ kHz. Results of these experiments are plotted in Fig. 9.

This figure shows ''rocking curves,'' i.e., the efficiencies of first-order Bragg diffraction, as a function of the incidence angle (angle of the retroreflection mirror), the same kind of measurement as performed in the previous experiment (see Fig. 4). The center of each plot corresponds to the static Bragg angle, i.e., the center peak always consists of elastically scattered atoms. As discussed above, side peaks at the left or right side of the center are due to atoms which increased or decreased their kinetic energy by one modulation quantum $\hbar\omega_M$ in the course of the diffraction process, respectively. The inset of each plot indicates the applied potential modulations of the two superimposed light crystals. As mentioned above, the absolute values of the two corresponding light potentials were equalized by adjusting the two superimposed crystals individually for equal relative diffraction efficiencies of about 20%.
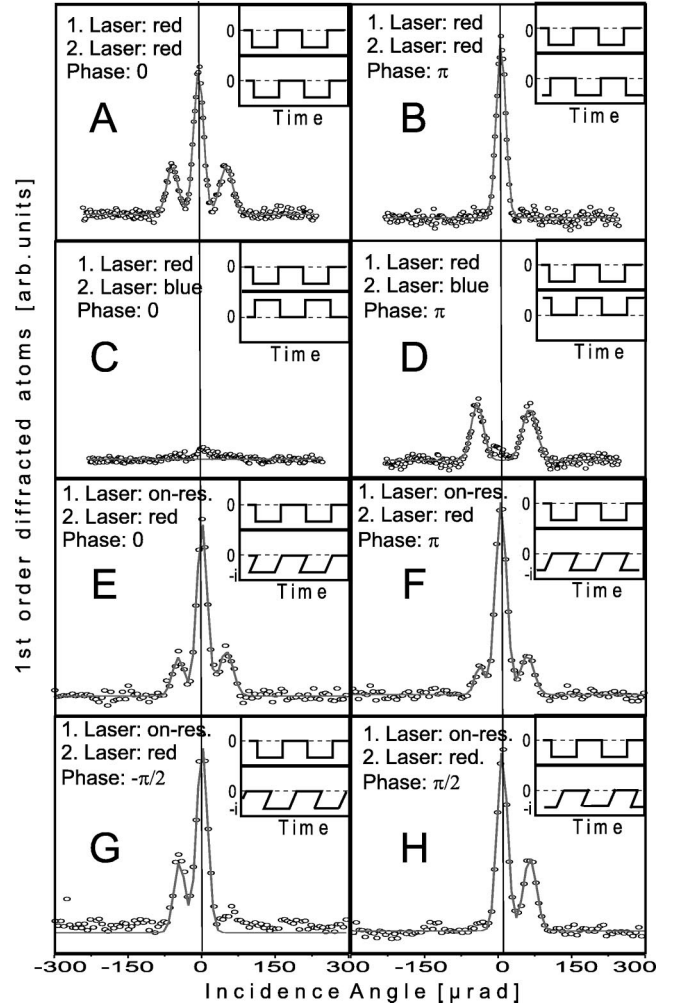


FIG. 9. Generation of atomic matter-wave sidebands with different potential modulation schemes. The figure shows the first-order diffraction efficiencies as a function of the crystal angle (''rocking curves''), for different temporal modulation functions. The time dependence of the two overlapping light crystal potentials are indicated in the insets. In (G) and (H), temporal potential modulations with a ''helicity in complex space'' result in completely asymmetric sideband generation.

In Fig. 9(a), the two lasers were both far detuned (ten linewidths) on the red side of the resonance line ($V_0$ is negative real, and $\phi_c = 0$), and they were switched on and off simultaneously ($\phi_t = 0$). The situation thus corresponds in effect to one single laser which is modulated. Therefore we obtain a result which is identical to the result of our ''basic'' sideband modulation experiment, sketched in the lower graph of Fig. 4, i.e., one central peak of elastically scattered atoms, and two side peaks of frequency-upshifted and -downshifted sidebands, respectively. The relative intensities of the four peaks should be 1:4:1, according to Eq. (26). However, it has to be mentioned that these quantitative estimates are only valid for small (relative) diffraction efficiencies. In the case of higher efficiencies, the sideband peaks are expected to gain efficiency with respect to the peak of elastically scattered atoms.

In Fig. 9(b), we performed a second control experiment,

by keeping the two lasers far red detuned ($V_0$ is negative real, and $\phi_c = 0$, as before), but by switching them on and off alternately ($\phi_t = \pi$), i.e., one laser was switched off when the other was switched on. In effect, this yields a constant, red detuned light field. Therefore, such an experiment corresponds to Bragg diffraction at an unmodulated static crystal, which yields only one peak of elastically scattered atoms at the Bragg angle, similar to the upper graph in Fig. 4. The suppression off the two side peaks is in agreement, with the predictions of Eq. (26).

In Fig. 9(c), the two lasers were detuned on different sides of the resonance line, i.e., the corresponding two light crystal potentials were positive real and negative real ($V_0$ is negative real, and $\phi_c = \pi$), respectively. The two lasers were modulated with equal phase ($\phi_t = 0$). As a result, scattering is completely suppressed. The reason for this is that the negative potential due to the red detuned laser and the positive potential due to the blue detuned laser cancel each other at any time. Therefore, no resulting crystal potential exists, and no scattering can be observed.

An interesting situation is sketched in Fig. 9(d), where the different detunings of the two lasers were the same as in the last experiment ($V_0$ is negative real, and $\phi_c = \pi$), but now the lasers were switched again alternately ($\phi_t = \pi$). Obviously, this results in a suppression of the static Bragg peak, whereas the sideband efficiencies are equal to the efficiencies in Fig. 9(a). The reason for the suppression of the static Bragg peak is that, during its passage through the crystal, each atom ''sees'' the crystal potential switch periodically between positive and negative values (each atom experiences about six switching periods inside the crystal). Therefore, on the time average, no crystal results, and no atoms can be elastically scattered. On the other hand, there exists a crystal potential which is modulated between positive and negative values, and which is thus able to generate sidebands. Quantitatively, Eq. (26) predicts the same sideband efficiencies as in Fig. 9(a), in agreement with our experimental result.

In the next parts of the experiment, we created a general complex potential modulation. This was achieved by combining a negative *imaginary* crystal potential (generated by tuning one of the lasers exactly on resonance) with a negative *real* potential (obtained by tuning the other laser on the far red side of the resonance frequency, i.e., $V_0$ is negative real, and $\phi_c = \pi/2$). The data of these experiments appear more noisy, since the total diffraction efficiency is drastically reduced with respect to the previous situations. The reason for this is that only about 10% of the incident atoms can pass the absorptive crystal. From these transmitted atoms, about 25% are diffracted at the first order (static diffraction), resulting in an absolute diffraction efficiency of only 2.5%. Furthermore, some of the metastable atoms ($\approx 28\%$), which should be absorbed after excitation by decaying to the ground state, rather decay spontaneously to their original metastable state, which contributes to some additional background. Nevertheless, the expected diffraction effects are clearly visible.

In Figs. 9(e) and in 9(f), the two lasers were switched on and off simultaneously [in Fig. 9(e), $\phi_t = 0$], and alternately [in Fig. 9(f), $\phi_t = \pi$], respectively. The results of the two
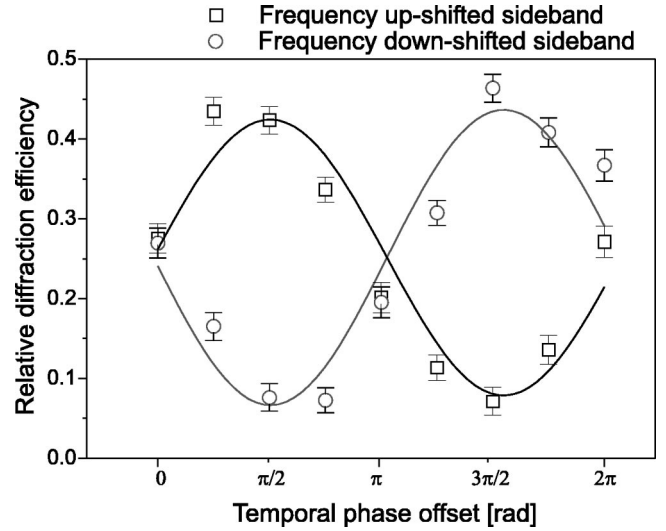


FIG. 10. Sideband generation efficiency as a function of the relative phase between the intensity modulations of two superimposed real and imaginary light crystal potentials.

experiments are approximately the same: They show two symmetric side peaks in addition to the central Bragg peak. The symmetric sideband generation in Figs. 9(e) and 9(f) is predicted by our model [Eq. (26)], as well as the symmetry between the two situations. The reason for this is that the sum and the difference of the relative temporal modulation phases $\phi_t$, and the complex phases $\phi_c$, in both situations yields only the values $-\pi/2$ or $+\pi/2$, which leads to no difference in the absolute values of the $P_{1,\pm 1}$ terms in Eq. (26). However, these are the only situations where a complex potential modulation leads to a symmetric sideband generation.

The sideband symmetry is maximally broken in the last two experiments [Figs. 9(g) and 9(h)], where the laser frequencies were the same as before, but the temporal intensity modulation phases were chosen to be $-\pi/2$ and $+\pi/2$, respectively. Obviously, this results in a suppression of one sideband and an enhancement of the other. The suppressed and enhanced sidebands are exchanged in the two experiments. This is due to the fact that both the temporal phase $\phi_t$ and the complex phase $\phi_c$ take the magnitude $\pi/2$. However, whereas the temporal phase enters into Eq. (26) with different signs for frequency-upshifted and -downshifted sidebands, the sign of the complex phase stays constant. Thus the two phases add to $\pi$ or cancel each other to 0 for the frequency-upshifted and -downshifted sidebands, respectively, resulting in a suppression or an enhancement of the respective peaks. According to Eq. (26) the efficiencies of the enhanced sideband should be approximately doubled with respect to the results of Figs. 9(e) and 9(f).

A more detailed investigation of the sideband efficiencies as a function of the relative temporal intensity modulation phase $\phi_t$ between the red detuned and the resonant lasers is presented in Fig. 10. The data indicate that the sideband efficiency depends sinusoidally on the relative modulation phase. Frequency-upshifted and -downshifted sidebands are created alternately, i.e., a suppression of one sideband is ac-

companied by a maximal efficiency of the other. All these observations confirm our model of sideband generation, and are in agreement with Eq. (26).

The extreme situations occur at relative modulation phases of $\pm \pi/2$, as already shown in Figs. 9(G) and 9(H). Investigating these situations in more detail, one finds that in these situations the temporal part of the potential modulation is of the form $V(t) \propto \exp(\pm i\omega_M t)$. Such an extremely non-Hermitian potential modulation represents a kind of helix in complex space, i.e., the modulus of the potential remains constant, whereas the complex phase rotates linearly as a function of time. The orientation of the helix is given by the sign of the exponent. Thus our experimental result suggests that such a temporally helical potential is only able to transfer energy in one direction, which depends on the orientation of the helix. Detailed analysis shows that a modulation of the form $\exp(-i\omega_M t)$ is able to emit energy in quanta of $\hbar \omega_M$, whereas an opposite orientation of the helix enables the potential to absorb energy quanta. Thus the normal symmetry between absorption and stimulated emission probabilities induced by time-varying fields is broken. The symmetry between absorption and stimulated emission is normally due to the fact that any real potential is Hermitian, which means that conjugate Fourier coefficients are pairs of complex conjugates, i.e., any contribution with negative helicity is accompanied by another contribution with positive helicity of the same intensity. This symmetry can only be broken in open systems, interacting with an environment which acts as a reservoir, since only in these cases the considered subsystem can be described by a non-Hermitian Hamiltonian.

Interestingly, an analogous effect was recently observed in the spatial domain [17]. In a similar setup a light crystal potential with a complex helicity in space was tailored, i.e., $V(x) \propto \exp(iGx)$. Although periodic, such a potential is very different from a real crystal potential [e.g., $V(x) \propto \cos(Gx)$], since the amplitude of the potential is constant at any point in space, though the complex phase changes. It has been observed that such a potential with complex helicity in space transfers a grating momentum $\hbar G$ only in one direction, i.e., the spatial diffraction pattern becomes asymmetric, similar to our actual experiment where a complex potential helicity in time transfers a modulation quantum $\hbar \omega_M$ only in one direction. Note that this analogy is not trivial, since the Schrö-dinger equation is not symmetric with respect to space and time coordinates.[4] Together, the two results clearly point out the role of non-Hermitian potential modulations, both in

_____

[4] One consequence of this is that it is always possible to change the direction of the atomic momentum without changing the energy (elastic scattering), but it is impossible to change the energy without adjusting the momentum. Therefore, in order to produce a frequency sideband by a temporal potential modulation, there always has to be an additional mechanism that provides the related momentum transfer. In our experiment we obtained this by combining temporal and spatial potential modulations, where the temporal part created the energy shift, and the spatial part supplied the related momentum change through its grating vector.

space and time, which give rise to asymmetric transfers of momentum or energy, respectively.

The asymmetric energy transfer in our actual experiment suggests an interesting practical application: Using such a modulation scheme it might be possible to cool a subsystem at the cost of its environment, which in our case would mean a cooling of the atoms in the metastable state at the cost of the atomic population in the ground state. However, here we have to mention that up to now this cannot be achieved in our system, since our potential modulation does not only consist of the desired complex helix, but also of a constant, negative imaginary term causing continuous absorption of the atoms. A working scheme for cooling thus will need a repumping transition, i.e., a resonance line which causes ''negative absorption'' (that is gain) at resonant excitation. In such a system, it is formally possible to generate a pure complex helical potential acting on one of the levels. Atoms in this level can then be cooled at the cost of the atoms in the other level, which acts as a reservoir.

### 2. Frequency-modulated complex light potential

In the following, we demonstrate a different approach to control the energy transfer to the diffracted atoms. In the preceding section, we showed how to control the time dependence of the complex potential by independently manipulating real and imaginary parts of the potential using superimposed on-resonant and off-resonant light fields. Now we show that a complementary method to manipulate a complex function, i.e., by directly controlling its magnitude and complex phase, can also be realized, and yields results that are in agreement with our model. In the following, we directly modulate the phase of the diffracted wave using the frequency dependence of the scattering phase, rather than Fourier synthesizing the frequency spectrum with different lasers, as before.

As already mentioned, the phase of the complex potential determines the phase of the scattered matter waves. This can be seen directly using the potential dependence of the diffracted wave *amplitude* given by Eq. (14) (valid for small diffraction efficiencies), allowing for a complex Pendellö-sung length given by Eq. (13). The spectral shape of the complex phase of a light potential near an atomic resonance line is plotted in Fig. 3. It corresponds to an arctangent function, with an offset of $-\pi/2$. Thus a phase shift of the scattered matter wave in a range of $-\pi$ to 0 can be achieved by just changing the light frequency in an interval ranging from the far red to the far blue detuned side of the absorption line. Thus we can achieve a phase modulation of the matter wave by modulating the light frequency, which can technically be achieved easily by modulating the current of a diode laser. Nevertheless, it has to be considered that, just by modulating the laser frequency without adjusting the light intensity, the amplitude of the light potential is also modulated. The complete spectral dependence of the amplitude and phase of the light potential is best expressed by reformulating Eq. (20):

$$V(\omega) = \frac{-i\hbar \Omega_{Rabi}^2/4}{\sqrt{(\omega - \omega_0)^2 + (\gamma/2)^2}} \exp\left[ i\arctan\left( \frac{\omega - \omega_0}{\gamma/2} \right) \right].$$

$$(27)$$

Here the first factor denotes the real amplitude, and the second factor the complex phase of the potential. The equation shows that a general modulation of the laser frequency, $\omega(t)$, yields a rather complicated modulation of the complex potential. Nevertheless, a controlled phase modulation can be achieved by simultaneously controlling the frequency and intensity of the laser light. One interesting kind of modulation is suggested by the arctangent dependence of the complex potential phase from the light frequency. If a periodic frequency modulation of the form

$$\omega(t) = \omega_0 + \frac{\gamma}{2} \tan(\omega_M t) \tag{28}$$

is applied, then this compensates for the arctangent spectral shape of the potential phase, and results in a linear phase shift as a function of time. Such a linearly changing phase shift just corresponds to a frequency offset of $\omega_M$, which is added to the matter-wave frequency. Such frequency generation, obtained by adding a linear phase shift, acts similarly to a Doppler frequency shift, obtained by reflecting a wave from a continuously moving object which also produces a linearly changing phase offset. The difference in our situation is that the phase shift cannot remain linear forever, since the tangent function is periodic. Therefore, the actual shape of the potential phase obtained by the frequency modulation of Eq. (28) becomes a sawtooth function of time, i.e., the phase changes linearly in an interval between $-\pi$ and 0, and then *jumps* back to its starting point. This corresponds exactly to the jump which the laser frequency has to perform at the poles of the tangent function in order to jump from one end of the resonance line to the other. The complete effect of this kind of frequency modulation can be seen if the modulation function [Eq. (28)] is inserted into the complex potential [Eq. (27)]. After some trigonometric manipulations we then obtain, for the time dependence of the modulated complex potential,

$$V(t) = \frac{-i\hbar\Omega_{Rabi}^2}{4\gamma}\cos(\omega_M t)\exp(i\omega_M t)$$

$$= \frac{-i\hbar\Omega_{Rabi}^2}{4\gamma}(1 + \exp(i2\omega_M t)). \tag{29}$$

This representation corresponds directly to a Fourier transform of the temporal potential modulation, i.e., there exist a static Fourier component and a component with frequency $2\omega_M$, with equal intensities. Therefore, this modulation is supposed to create both elastically scattered atoms and a single frequency sideband offset by $-2\omega_M$. Note that the sideband frequency offset deviates from the modulation frequency $\omega_M$. This is due to the phase jump after each phase change of $\pi$ in the tangent function (which performs two oscillations in an interval of $2\pi$). Therefore, the actual frequency of the modulation is in fact $2\omega_M$, although the argument of the tangent function is only $\omega_M t$.

In order to experimentally investigate the effects of laser-frequency modulations, we used the same setup as sketched in Fig. 2, with one single diode laser (without any acousto-
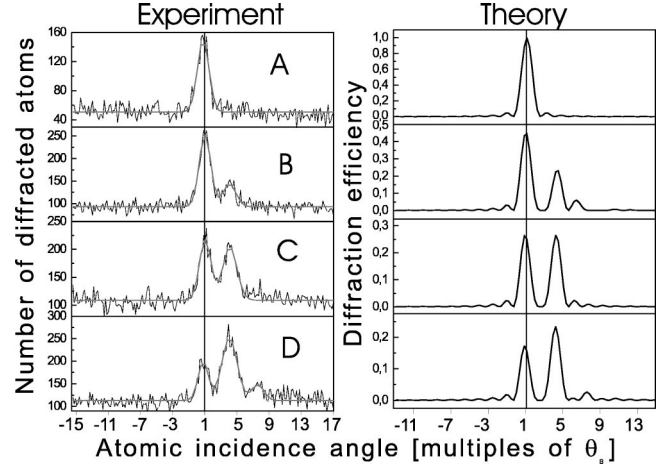


FIG. 11. Experimental realization of a lopsided frequency shifter using a frequency-modulated light crystal. In the different plots, a tangent-shaped frequency modulation function ($\omega_M = 2\pi \times 50$ kHz) according to Eq. (28) was applied, with different slopes of 0, 3.5 MHz, 7 MHz, and 10 MHz, respectively. The slopes correspond to the prefactor $\gamma/2$ in Eq. (28). The experimental results are reproduced by the numerical calculations of the Fourier composition (squared absolute values) of the potential modulations (right side of the graph).

optic modulator). The laser frequency could be modulated by driving the diode laser current with a programmable signal generator. The frequency offset obtained by changing the laser current was measured with a Fabry-Perot spectrum analyzer.

In the experiment we demonstrate that a tangent-shaped frequency modulation function according to Eq. (28) produces only one single sideband of either frequency-upshifted or frequency-downshifted atoms. This is done in a sequence of experiments where we successively increased the slope of the tangent function by increasing the amplitude of the tangent shaped frequency modulation (Fig. 11). The results are compared with numerical calculations, where the squared absolute values of the respective Fourier coefficients of the potential modulation (convoluted with a phenomenological line-shape function) were computed. Note that the preceding analytic calculation holds only for a modulation function which is exactly the inverse function of the argument in Eq. (27). Since we were now using different slopes of the tangent function, the calculation of the Fourier composition became more complicated and is done numerically.

In the experiment the laser frequency was modulated with a frequency $\omega_M = 50$ kHz across the 801.7-nm open atomic transition line. Nevertheless, as mentioned above, the actual frequency of the laser sweep across the resonance line was 100 kHz, since the tangent function is already periodic in an interval of $\pi$. The laser frequency was centered at the resonance line and then periodically modulated in the shape of a smooth tangent function from the red to the blue side of the resonance, followed by a sudden jump back. The frequency interval in which the laser was swept was about $\pm 5$ linewidths across the resonance frequency. The first-order diffraction efficiency was measured again as a function of the crystal angle (''rocking curves''). The upper graph [Fig.

11(a)] shows a rocking curve obtained at an unmodulated light crystal. The peak of elastically scattered atoms denotes the position of the Bragg angle. In Figs. 11(b), 11(c), and 11(d), the light frequency was modulated symmetrically across the atomic resonance frequency according to Eq. (28) with increasing amplitude of the tangent function.

In any case, new Bragg peaks are found only on one side of the static Bragg peak, indicating that the potential modulation can produce only lop-sided energy shifts. In Fig. 11(c) the peaks of elastically scattered atoms and frequency shifted atoms have approximately equal intensities, as predicted by Eq. (29) for a slope of the tangent function of $\gamma/2 \approx 4.5$ MHz (the theoretical linewidth of the 801.7-nm transition is $\gamma \approx 9$ MHz), which should result in a sawtooth phase shift of the complex potential phase as a function of time. As expected from the Fourier representation of the potential in Eq. (29), we obtain only one side peak of atoms shifted by twice the modulation frequency ($2 \times 50$ kHz). However, our actually applied slope in this experiment was 7 MHz. The difference might be due to a change in the *effective* linewidth by saturation effects when scanning the laser frequency across resonance, or to an increased linewidth of the laser generated by its fast modulation.

In the other parts of the experiment it is shown that smaller slopes of the modulation result in smaller sideband efficiencies [Fig. 11(b)], whereas larger slopes [Fig. 11(d)] create increased sidebands, while simultaneously populating higher sideband orders (a small additional side peak). The experimental results are in agreement with the numerical calculations plotted on the right side, which represent the squared value of the Fourier composition of the potential modulation functions [there an effective linewidth $\gamma = 14$ MHz is assumed, as suggested by the symmetric result in Fig. 11(c)].

We also checked the effect of flipping the sign of the tangent function, which resulted, as expected, in a sideband peak with a different sign of the frequency offset, i.e., a peak at the other side of the central Bragg peak. This means that scanning across an atomic transition line from the red side to the blue side yields different results as compared to the reverse direction. This symmetry violation is due to the spectral shape of the complex interaction potential determined by the Kramers-Kronig dispersion relations, and thus fundamentally based on causality.

Note that although the resulting asymmetric sidebands look similar to those in the previous experiment where we used independent modulations of real and imaginary parts of the potential, the principle is different. Actually, the phase relation between the generated single sideband and the static Bragg peak also differs in the two situations, which might be demonstrated in an interferometric experiment.

The demonstrated method to produce an asymmetric sideband has an analogy in the spatial domain [26]. The method resembles the principle of a blazed grating in space. Such a blazed grating has a sawtooth spatial profile. This profile is embossed on an incident plane wave front, i.e. the wave front acquires a sawtooth phase shift. In the ideal case, the spatial phase changes in a range of $2\pi$, and then jumps back to 0. In this case the blazed grating has the property to diffract an

incoming wave exclusively at one spatial diffraction order, but not at the conjugate order. This is in contrast to a normal phase grating, consisting of a harmonic periodic phase modulation, which diffracts symmetrically at conjugate orders. Very similarly, in our experiment we imprinted a time-dependent phase shift at an incoming matter wave, resulting in frequency sideband production. By applying a time-dependent periodic phase shift with the shape of a sawtooth function, which we obtain as a result of our tangent modulation, we observe only one sideband of the atomic matter wave. Thus our experiment transfers in a certain sense the principle of a spatially blazed grating to the time domain of atomic matter waves. Although the analogy is not completely perfect,[5] this viewpoint helps to understand the principle of operation, and suggests building time analogs to other elements of standard diffractive optics, like a ''Fresnel lens in time.''

### 3. Bloch band spectroscopy

Here we briefly sketch an alternative model for the diffraction behavior of the argon atoms in the modulated standing light field, which opens up a different viewpoint and points out the relation of our experiments to recently performed investigations of atoms in optical traps. In addition to the extended Ewald model, our experiments can be interpreted as a kind of spectroscopy of the Bloch bands which describe the dynamic behavior of a particle in a periodic potential. Recently, this viewpoint was used advantageously to model test systems for demonstrating some quantum effects predicted in solid-state physics for electronic transport in periodic crystals, which were hard to demonstrate in condensed-matter systems [5,4,7]. In our case, the model shows that our complex potential modulations can induce directed transitions between energy levels—an effect that is ''normally'' forbidden with ''ordinary'' (Hermitian) potentials, due to basic concepts of quantum mechanics.

A one-dimensional band-structure description of the atoms in a crystal is sketched in Fig. 12. Bloch bands in a weakly modulated spatially periodic system are formed by repeating the free-particle dispersion parabola (indicated by a dashed line in the figure), which is normally centered at zero momentum, at distances given by the grating vector $\vec{G}$, since in periodic systems all momenta are only defined up to multiples of the fundamental grating momentum $\hbar\vec{G}$. The influence of quantum mechanics is, then, to split and reconnect

---

[5]Our lopsided frequency shifter is not a perfect analog to a spatially blazed grating, since it still produces a residual peak of elastically scattered atoms. This would correspond to a blazed grating in space, which diffracts only 50% of the incoming wave. However, the deviation from the ideal behavior can be attributed to the fact that we can change the temporal matter-wave phase by our frequency modulation only in an interval of $\pi$ instead of the ideally required interval of $2\pi$. Similarly, a spatial sawtooth phase grating which changes the phase of a wave front only in an interval of $\pi$ would have the property to diffract only 50% of the wave at one order.
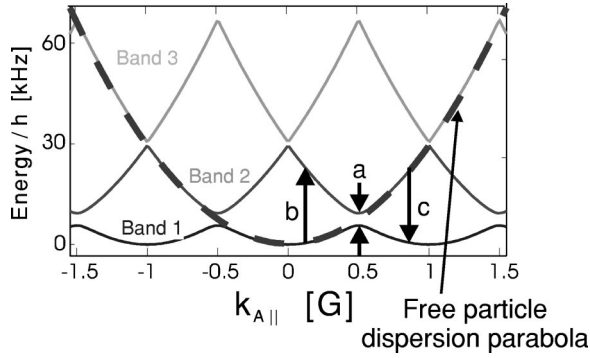
FIG. 12. Band structure of atomic matter waves in a one-dimensional light crystal. Transitions within the band structure (arrows *b* and *c*) are induced by a resonant perturbation, and result in new Bragg peaks of frequency-shifted atoms.

the individual parabolas at their crossing points, such that bands are formed. However, for weak modulation the underlying structure of periodically repeated free-particle parabolas is still clearly expressed, and, actually only broken in an area closely surrounding the crossing points. In Fig. 12 the corresponding atomic eigenenergies are plotted as a function of the atomic wave-vector component $k_{A\parallel}$ parallel to the grating vector $\vec{G}$. Therefore, in our case of small incidence angles (paraxial geometry), the *x* axis is directly proportional to the atomic incidence angle ($k_{A\parallel} \approx |\vec{k}_A| \theta$). The dashed parabola indicates the dispersion of a free atom outside of the crystal. At the crystal boundary the originally free atoms are coupled into the particular crystal bands which coincide with their free (kinetic) energy parabola. Since this free parabola at most positions directly overlaps with the crystal bands, the resulting population of the bands is obvious: e.g., the lowest Bloch band is populated for atomic incidence angles between 0 (perpendicular incidence) and $\theta_B$, the next band in a range between $\theta_B$ and $2\theta_B$, and so on. At incidence angles which are far enough separated from the (prevented) crossing points, the corresponding eigenfunctions simply consist of (almost) free plane waves that correspond to the incident wave. Only in cases where the free atomic parabola crosses a band gap is it possible to populate two Bloch bands simultaneously, for example at position *a* in Fig. 12. The two corresponding eigenfunctions at these positions consist of two sinusoidally modulated wave functions. Their corresponding intensity distributions form two copies of the crystal grating, with a relative phase shift of $\pi$ with respect to each other [16], i.e., one of the atomic intensity gratings directly coincides with the crystal potential, whereas the other is exactly out of phase. In these special cases, the energy gap between the two populated bands leads to a different time evolution of the two corresponding atomic wave functions. Recombination of these two wave functions at the rear boundary of the crystal then results in *two* outgoing propagation directions, i.e. a transmitted and a Bragg-diffracted beam. Thus the (prevented) crossing points of adjacent parabola correspond to the Bragg angles. These crossing points appear at the positions (see Fig. 12): $k_{A\parallel} = nG/2$, resulting in the standard Bragg condition $\theta_B \approx nG/2k_A$.

So far the preceding illustrations were a qualitative picture of the predictions of dynamical diffraction theory, as originally developed for diffraction of x rays, electrons, and neutrons at solid crystals [27]. Applied to our situation of scattering at a modulated crystal, this model suggests an alternative explanation for the appearance of the new Bragg peaks in the "rocking curves." There the potential modulation is assumed to be a resonant perturbation.[6] Even atoms, which enter the crystal far from a Bragg angle, and thus occupy only one crystal band, can be excited by this time-dependent resonant perturbation into a superposition of two bands (e.g., arrows *b* or *c* in Fig. 12), and successively scattered. This results in a Bragg diffraction of coherently frequency shifted matter waves. From the band symmetries it is obvious that resonant transitions to higher (e.g., arrow b) and lower bands (e.g., arrow c) are arranged symmetrically around the static Bragg angles (e.g., position a), which explains the symmetric distribution of the new Bragg peaks in the rocking curves of Fig. 4. Calculating the vertical distances between two bands in a region far from a band gap can be done by just determining the energy difference between the corresponding two horizontally displaced free-particle parabolas (since these parabolas are only disturbed in the region very close to a static Bragg angle, i.e., at a band gap). This straightforward calculation delivers the same result for the modulation frequencies belonging to the new Bragg angles, as our generalized Ewald model.

The above viewpoint also indicates that our experiments are a direct spectroscopic method to measure the Bloch band structure of the light crystal. In contrast to previously described methods of Bloch band spectroscopy in atomic traps [6], the well-collimated beam of incoming atoms is generally coupled only into one single band (with the exception of the static Bragg angles), and even this band is populated only at a specific momentum position, which can be controlled directly by adjusting the incidence angle. Starting from this well-defined position the temporal modulation induces a direct resonant transition to an upper or lower band, which is indicated by the appearance of a new Bragg peak at the respective side of the static peak. Thus scanning the modula-

––––––––––

[6]It might be striking that a fully modulated crystal potential is treated here as a perturbation. However, as explained above, the main structure of the crystal bands is just given by repeating free-particle parabola at distances of a grating vector $G$. Thus the most important property is only determined by the periodicity of the crystal, but not by the absolute potential strength (as long as an adiabatic evolution of the atomic wave function in a band is possible). The only property influenced by the potential strength is the splitting (and the eigenfunctions) in the region very close to the band-gap positions (in the case of small enough potentials, which is automatically fulfilled if the crystal shows Bragg diffraction peaks with a high angular selectivity). However, in our modulation experiments we are mainly interested in atoms far from the band gaps, i.e., at positions where the originally free atomic wave function is almost uninfluenced by the crystal in any case. There, in fact, the crystal intensity modulation acts only as a small perturbation, even if the crystal potential is modulated with an amplitude of 100%.

tion frequency or the incidence angle measures the distance between Bloch bands with high accuracy (note that the typical transition energy $\hbar\omega_M$ is in our case about ten orders of magnitude lower than the kinetic energy of the atoms).

This viewpoint also implies that the asymmetric sideband generation demonstrated in Sec. II is in fact a lopsided transition between two crystal bands. The creation of only one sideband in such an energy-level scheme means that only one of the indicated transitions (e.g., arrow b) can be induced by the potential modulation, whereas the same modulation cannot drive the corresponding symmetric transition (arrow c), although the modulation frequency is resonant with both transitions. The reason for this behavior is the temporal helicity of the complex potential modulation. As mentioned above, such an absorption without stimulated emission (or vice versa) within the band structure of an optical lattice suggests applications like a cooling of the atoms to the ground state.

## IV. OUTLOOK

We have demonstrated that sidebands of atomic matter waves can be produced by diffraction at intensity- or frequency-modulated light crystals, either by directly modulating real and imaginary parts of the light potential or by modulating its amplitude and complex phase. The effect can be characterized as a coupled spatial and temporal Bragg diffraction process. Specific non-Hermitian potential modulations can have the shape of a time-dependent complex helix. These modulations transfer energy only in one direction, i.e., either to lower or higher values, and thus violate the usual symmetry between absorption and stimulated emission of energy quanta. This is an interesting analog to a recently demonstrated asymmetric *momentum* transfer which occurs when atoms are diffracted at complex potentials with *spatial* helicity [17].

The investigated temporal diffraction effects imply many interesting applications. For example, the asymmetric energy transfer produced by non-Hermitian potential modulations might be used for cooling atoms to the ground state of an optical lattice, or to gain complete control over the atomic population of the energy bands. In this case it is necessary to chose an atomic system which allows for a repumping of the ground-state atoms to the metastable state.

Furthermore, the sideband modulation techniques now enable many applications, which have been advantageously used in light optics and in radio-frequency technology, to be transferred into an analogous matter-wave technology. Con-

trolled modulation, or frequency shift of matter waves can be used in atomic interferometry, in order to build active Mach-Zehnder-type atom interferometers [18,19], where the coherent wave splitters and recombiners consist of modulated light gratings. These are promising tools for high-precision rotation or gravitation sensors [39]. For example, using the described modulation techniques, it is possible to impress a precisely controlled de Broglie frequency difference at the atoms in the two paths of an atom interferometer. This allows highly increased sensitivity by lock-in detection of the oscillating interference fringes, or by actively tracking the interference phase with a changing frequency difference. In more advanced experiments this might also enable the interferometric detection of mass- or velocity-dependent dispersion phenomena, which are expected in certain atomic scattering and collision processes, in magnetic fields, or in gravitation physics.

Another application in sophisticated measurement technology is the use of modulated standing light fields for precise mass spectroscopy of atomic or molecular beams. There a particle beam crosses a thick modulated standing light wave at exactly perpendicular incidence. By scanning the intensity modulation frequency of the light crystal, diffraction peaks will appear only at specific modulation frequencies (the two-photon recoil frequency), which depend only on the particle mass and the precisely measurable light frequency, but not at hardly controllable parameters like the particle velocities. Using an intense laser the optical frequency can be selected over a wide range around atomic or molecular transition lines, since the refractive potential of the light field falls off only slowly with increasing frequency difference from resonance.

In fundamental research, the control over the sideband structure of atoms can be used to investigate the quantum mechanics of atomic wave packets, an exciting field of quantum optics. Advanced technologies in laser optics, like chirping and compression of laser pulses, which are important techniques for achieving ultrashort pulses, might also be emulated advantageously with modulated matter waves. These experiments have now become feasible, since degenerate quantum gases of atoms are readily obtainable as coherent sources of atomic matter waves.

## ACKNOWLEDGMENTS

[1] M. Weidemüller, A. Görlitz, T. W. Hänsch, and A. Hemmerich, Phys. Rev. A **58**, 4647 (1998); M. Weidemüller, A. Hemmerich, A. Görlitz, T. Esslinger, and T. W. Hänsch, Phys. Rev. Lett. **75**, 4583 (1995); A. Hemmerich, M. Weidemüller, T. Esslinger, C. Zimmermann, and T. W. Hänsch, Phys. Rev. Lett. **75**, 37 (1995).

[2] C. Mennerat-Robilliard, D. Lucas, S. Guibal, J. Tabosa, J.-Y. Courtois, and G. Grynberg, Phys. Rev. Lett. **82**, 851 (1999); S.

Guibal, C. Mennerat-Robillard, D. Larousserie, C. Triche, J.-Y. Courtois, and G. Grynberg, *ibid.* **78**, 4709 (1997).

[3] F. L. Moore, J. C. Robinson, C. F. Bharucha, Bala Sundaram, and M. G. Raizen, Phys. Rev. Lett. **75**, 4598 (1995).

[4] M. B. Dahan, E. Peik, J. Reichel, Y. Castin, and C. Salomon, Phys. Rev. Lett. **76**, 4508 (1996); E. Peik, M. B. Dahan, I. Bouchoule, Y. Castin, and Ch. Salomon, Phys. Rev. A **55**, 2989 (1997).

[5] S. R. Wilkinson, C. F. Bharucha, K. W. Madison, Quian Niu, and M. G. Raizen, Phys. Rev. Lett. **76**, 4512 (1996); Quian Niu, Xian-Geng Zhao, G. A. Georgakis, and M. G. Raizen, Phys. Rev. Lett. **76**, 4504 (1996).

[6] K. W. Madison, M. C. Fischer, R. B. Diener, Quian Niu, and M. G. Raizen, Phys. Rev. Lett. **81**, 5093 (1998); M. C. Fischer, K. W. Madison, Quian Niu, and M. G. Raizen, Phys. Rev. A **58**, R2648 (1998).

[7] T. Müller-Seydlitz *et al.*, Phys. Rev. Lett. **78**, 1038 (1997).

[8] S. B. Cahn, A. Kumarakrishnan, U. Shim, T. Sleator, P. R. Berman, and B. Dubetsky, Phys. Rev. Lett. **79**, 784 (1997).

[9] S. N. Chormaic, S. Franke, F. Schmiedmayer, and A. Zeilinger, Acta Phys. Slov. **46**, 463 (1996).

[10] P. L. Gould, G. A. Ruff, and D. E. Pritchard, Phys. Rev. Lett. **56**, 827 (1986).

[11] P. J. Martin, B. G. Oldaker, A. H. Miklich, and D. E. Pritchard, Phys. Rev. Lett. **60**, 515 (1988).

[12] D. M. Giltner, R. W. McGowan, and S. A. Lee, Phys. Rev. A **52**, 3966 (1988).

[13] S. Dürr, S. Kunze, and G. Rempe, Quantum Semiclassic. Opt. **8**, 531 (1996).

[14] S. Dürr and G. Rempe, Phys. Rev. A **59**, 1495 (1999).

[15] M. K. Oberthaler, R. Abfalterer, S. Bernet, J. Schmiedmayer, and A. Zeilinger, Phys. Rev. Lett. **77**, 4980 (1996).

[16] M. K. Oberthaler, R. Abfalterer, S. Bernet, C. Keller, J. Schmiedmayer, and A. Zeilinger, Phys. Rev. A **60**, 456 (1999).

[17] C. Keller, R. Abfalterer, S. Bernet, M. K. Oberthaler, J. Schmiedmayer, and A. Zeilinger, Phys. Rev. Lett. **79**, 3327 (1997).

[18] D. M. Giltner, R. W. McGowan, and S. A. Lee, Phys. Rev. Lett. **75**, 2638 (1995).

[19] E. M. Rasel, M. K. Oberthaler, H. Batelaan, J. Schmiedmayer, and A. Zeilinger, Phys. Rev. Lett. **75**, 2633 (1995).

[20] B. P. Anderson and M. A. Kasevich, Science **282**, 1686 (1998).

[21] M. Kozuma, L. Deng, E. W. Hagley, J. Wen, R. Lutwak, K. Helmerson, S. L. Rolston, and W. D. Phillips, Phys. Rev. Lett. **82**, 871 (1999).

[22] J. Stenger, S. Inouye, A. P. Chikkatur, D. M. Stamper-Kurn, D. E. Pritchard, and W. Ketterle, Phys. Rev. Lett. **82**, 4569 (1999).

[23] S. Bernet, M. Oberthaler, R. Abfalterer, J. Schmiedmayer, and A. Zeilinger, Quantum Semiclassic. Opt. **8**, 497 (1996).

[24] S. Bernet, M. K. Oberthaler, R. Abfalterer, J. Schmiedmayer, and A. Zeilinger, Phys. Rev. Lett. **77**, 5160 (1996).

[25] S. Bernet, R. Abfalterer, C. Keller, J. Schmiedmayer, and A. Zeilinger, Proc. R. Soc. London, Ser. A **455**, 1509 (1999).

[26] S. Bernet, R. Abfalterer, C. Keller, J. Schmiedmayer, and A. Zeilinger, J. Opt. Soc. Am. B **15**, 2817 (1998).

[27] See, e.g., B. W. Batterman and H. Cole, Rev. Mod. Phys. **36**, 681 (1964); H. Rauch and D. Petrascheck, in *Neutron Diffraction*, edited by H. Dachs (Springer, New York, 1978), p. 303; M. A. Horne, K. D. Finkelstein, C. G. Shull, A. Zeilinger, and H. J. Bernstein, in *Matter Wave Interferometry*, edited by G. Badurek, H. Rauch, and A. Zeilinger (North-Holland, Amsterdam, 1988), p. 189.

[28] H. Kogelnik, Bell Syst. Tech. J. **48**, 2909 (1969).

[29] Ch. J. Bordé, in *Atom Interferometry*, edited by P. E. Berman (Academic Press, New York, 1997).

[30] D. O. Chudesnikov and V. P. Yakovlev, Laser Phys. **1**, 110 (1991).

[31] M. Moshinsky, Phys. Rev. **88**, 625 (1952); M. Moshinsky, Am. J. Phys. **44**, 1037 (1975).

[32] A. Steane, P. Szriftgiser, P. Desibiolles, and J. Dalibard, Phys. Rev. Lett. **74**, 4972 (1995); P. Szriftgiser, D. Guéry-Odelin, M. Arndt, and J. Dalibard, Phys. Rev. Lett. **77**, 4 (1996).

[33] J. Felber, R. Gähler, C. Rausch, and R. Golub, Phys. Rev. A **53**, 319 (1996); G. Badurek, H. Rauch, and D. Tuppinger, Phys. Rev. A **34**, 2600 (1986).

[34] D. E. Pritchard and P. L. Gould, J. Opt. Soc. Am. B **2**, 1799 (1985).

[35] P. E. Moskowitz, P. L. Gould, S. R. Atlas, and D. E. Pritchard, Phys. Rev. Lett. **51**, 370 (1983).

[36] Our experimental setup was described in detail by H. Batelaan *et al.*, in *Atom Interferometry* (Ref. [29]).

[37] M. V. Berry and D. H. J. O'Dell, J. Phys. A **31**, 2093 (1998).

[38] M. V. Berry, J. Phys. A **31**, 3493 (1998).

[39] M. K. Oberthaler, S. Bernet, E. M. Rasel, J. Schmiedmayer, and A. Zeilinger, Phys. Rev. A **54**, 3165 (1996).